


# Photoionized Herbig-Haro objects in the Orion Nebula II: HH 204

J. E. Méndez-Delgado<sup>1,2</sup> , C. Esteban<sup>1,2</sup>, J. García-Rojas<sup>1,2</sup>, W. J. Henney<sup>3</sup>  
and collaborators

<sup>1</sup>*Instituto de Astrofísica de Canarias (IAC), E-38205 La Laguna, Spain*

<sup>2</sup>*Departamento de Astrofísica, Universidad de La Laguna, E-38206 La Laguna, Spain*

<sup>3</sup>*Instituto de Radioastronomía y Astrofísica, Universidad Nacional Autónoma de México, Apartado Postal 3-72, 58090 Morelia, Michoacán, México*

Accepted XXX. Received YYY; in original form ZZZ

## ABSTRACT

This is the abstract.

**Key words:** ISM:Abundances – ISM: Herbig–Haro objects – ISM: individual: Orion Nebula – ISM: individual: HH 204.

## 1 INTRODUCTION

HH 204 is a Herbig-Haro (HH) object located in the central region of the Orion Nebula, just at the southeast of the Orion Bar, apparently close to the  $\theta^2$  Ori A star. It was observed by Münch & Wilson (1962) and classified as an HH by Canto et al. (1980). The origin of the jet is associated with the Orion South molecular cloud (Orion-S) (O’Dell et al. 2017a), an active star formation area of the Orion Nebula. It is photoionized by  $\theta^1$  Ori C from behind its direction of propagation, through the cavity formed by the shock (O’Dell et al. 1997b, 2017a). There are several works dedicated to this object and the neighboring HH 203 (Doi et al. 2004; Henney et al. 2007; García-Díaz et al. 2008; O’Dell et al. 2015, and references therein), investigating their proper motions, structure and kinematics of the zone of the Orion Nebula where the shock takes place. Through long-slit spectra, Mesa-Delgado et al. (2008) studied the effects of HH 204 on the gas of the Orion Nebula, finding peaks in the density and temperature distributions when crossing its zone of influence as well as increases in the emission flux of [Fe III] lines produced by dust destruction. Using integral field spectroscopy, Núñez-Díaz et al. (2012) studied the influence of HH 204 in the Orion Nebula in an area  $16 \times 16$  arcsec<sup>2</sup>, finding the presence of a trapped ionization front as well as arguments in favor of the location of the object within the main body of the Orion Nebula and not in the Veil. The works by Mesa-Delgado et al. (2008), Núñez-Díaz et al. (2012) and O’Dell et al. (2017a) show the presence of a high- $T_e$  ([N II]) zone, attributed to shock heating. However, this effect and the coincidental fall in the total abundance of O, may be related with an underestimation of  $n_e$ , an alternative explanation that will be discussed here.

This is the second article in a series dedicated to study photoionized HH objects in the Orion Nebula using high-resolution spectroscopy obtained with the Ultraviolet and Visual Echelle Spectrograph (UVES) (D’Odorico et al. 2000) of the Very Large Telescope (VLT). In this work, we analyze the physical conditions, chemical composition and physical properties of HH 204, separating the

emission of the Orion Nebula from the HH objects and other ionized gas components present in the line of sight. Previous to the present work, the number of works dedicated to high-resolution spectroscopy of photoionized HH objects of the Orion Nebula has been very short, dedicated to HH 202 S (Mesa-Delgado et al. 2009), HH 529 II and HH 529 III (Blagrove et al. 2006; Mendez Delgado & Amigos 2021). This article has the following content: in Sec. 2 we describe the observational data and its treatment. In Sec. 3 we describe the measurement of the spectral lines and the reddening correction. In Sec. 4 we derive the physical conditions and the ionic abundances of each of the observed velocity components, while in Sec. 5 we focus exclusively in HH 204 deriving their physical conditions, ionic abundances and some properties pixel-by-pixel along the observed area. In Sec. 6 we estimate the total abundances of the observed gas components. In Sec. 7 we study the effects of mixing three gas components of very different density along the line of sight, simulating a spectrum with lower spectral resolution. In Sec. 8 we discuss the main results of this work and their implications. Finally, in Sec. 9 we summarize the conclusions. In the Appendix, tables of data and figures are added as support material.

## 2 OBSERVATIONS AND DATA REDUCTION

The observations were made during the night of October 28 and 29, 2013 under photometric conditions using UVES in the UT2 of the Very Large Telescope (VLT) in Cerro Paranal, Chile. The slit position was centred at the coordinates RA(J2000)=05<sup>h</sup>35<sup>m</sup>22<sup>s</sup>.72, DEC(J2000)=−05°25′20.42″ with a parallactic angle of 137°. The slit width provides an effective spectral resolution  $\lambda/\Delta\lambda \approx 6.5$  km s<sup>−1</sup>, covering the spectral range between 3100–10420 Å. Three exposures of 150s of the standard star GD71 (Moehler et al. 2014a,b) were taken in the same night under similar observational conditions than the science images to achieve the flux calibration of the data. The observational settings are shown in Table 1 and the spatial coverage is presented in Fig. 1. The instrumental configuration and the data reduction procedure is described in Mendez Delgado

\* E-mail: jemd@iac.es



**Figure 1.** Composite WFC2 *HST* image of the region southeast of the Bright Bar of the Orion Nebula. Three narrow filters were used for the color scale: F502N, F658N and F656N for red, green and blue, respectively (images obtained by Bally et al. 1998). The slit position of our observations is indicated.

& Amigos (2021) (hereinafter Paper I). The 2D spectra (see Fig. 2) shows three evident components: the nebular one (the emission of Orion Nebula), which is rather homogeneously distributed along the spatial axis of the slit and occupies the reddest spectral position; the “Blue Layer”, a slightly blueshifted homogeneous diffuse component previously detected by Deharveng (1973) that may correspond to a different H II region along the same line of sight (García-Díaz & Henney 2007) and HH 204, the “ball-shaped” bluest component. We define two spatial cuts as it is shown in Fig. 2, covering a spatial area of 7.38 arcsec for cut 1 and 1.97 arcsec for cut 2. In cut 2, we can separate the emission of the Blue Layer and the nebular component. However, due to the strong contribution of HH 204, we can not separate those components in cut 1. In this case, we study the emission of the combined spectrum of the nebular component and the Blue Layer. We also take advantage of the quality of the data performing a pixel-by-pixel analysis of various emission lines in order to detect small changes in physical conditions and/or the chemical composition in HH 204 along the slit.

**Table 1.** Main parameters of UVES spectroscopic observations.

Date	$\Delta\lambda$ (Å)	Exp. time (s)	Seeing (arcsec)	Airmass
2013-10-29	3100-3885	5, 3×180	0.85	1.11
2013-10-29	3750-4995	5, 3×600	0.70	1.16
2013-10-29	4785-6805	5, 3×180	0.85	1.11
2013-10-29	6700-10420	5, 3×600	0.70	1.16

### 3 LINE INTENSITIES AND REDDENING

We use SPLIT task from IRAF to measure the line intensities and estimate their uncertainties as it is described in detail in Paper I. In the case of the spectra of cut 1 and cut 2, we measure a complete set of around 520 and 310 emission lines (falta contarlas por componente), respectively, while in the case of the pixel-by-pixel measurements for HH 204, we restrict ourselves to some representative lines: H9, H $\beta$ , H $\alpha$ ; He I  $\lambda\lambda$ 4471.47, 5875.64, 6678.15; [N II]  $\lambda\lambda$ 5754.64, 6583.46; O I  $\lambda$ 7771.94; [O I]  $\lambda$ 6300.30; [O II]  $\lambda$ 3726.03; [O III]  $\lambda\lambda$ 4363.21, 4958.91; [Ne III]  $\lambda$ 3868.75; [S II]  $\lambda\lambda$ 6716.44, 6730.82; [S III]  $\lambda\lambda$ 6312.10, 9530.60; [Cl II]  $\lambda$ 9123.60; [Cl III]  $\lambda$ 5537.88; [Ar III]  $\lambda$ 7135.80; [Ca II]  $\lambda$ 7323.89; [Cr II]

**Table 2.** Reddening coefficients for each component.

$c(H\beta)$		
	HH 204	Nebula+Blue Layer
Cut 1	$0.42 \pm 0.02$	$0.31 \pm 0.03$
	Blue Layer	Nebula
Cut 2	$0.42 \pm 0.09$	$0.30 \pm 0.04$

$\lambda 8000.08$ ; [Fe II]  $\lambda 9051.95$ ; [Fe III]  $\lambda \lambda 4658.17, 4701.64, 4881.07$ ; [Ni II]  $\lambda 7377.83$  and [Ni III]  $\lambda 7889.93$ . The reddening correction was done using the extinction curve from [Blagrove et al. \(2007\)](#) and the emissivity coefficients of [Storey & Hummer \(1995\)](#) for H $\epsilon$ , H $\delta$ , H $\gamma$ , H $\beta$  and H $\alpha$  Balmer lines and the P12, P11, P10, P9 Paschen lines. The values of the extinction coefficient,  $c(H\beta)$ , are presented in Table 2. In the case of pixel-by-pixel measurements, a value of  $c(H\beta) = 0.42 \pm 0.02$  was used.

## 4 ANALYSIS OF INTEGRATED SPECTRA OF EACH COMPONENT

### 4.1 Physical Conditions

We use the version 1.1.13 of PyNeb ([Luridiana et al. 2015](#)) to obtain the physical conditions of the gas from the intensity ratios of Collisional Excited Lines (CELs) and Recombination Lines (RLs). PyNeb is a python based tool to compute line emissivities and derive physical conditions and chemical abundances of ionized gas. We have used the atomic data set used presented in Table A4 and Table A5 for the calculations made with PyNeb. We first estimate the electron density,  $n_e$ , given by each diagnostic of CELs by calculating each convergence of  $T_e - n_e$  with the available  $T_e$  diagnostics, using the PyNeb task *getCrossTemDen*, as it is described in detail in Paper I. Then, in the nebular and Blue Layer components, we adopt the weighted mean<sup>1</sup> of the available values of  $n_e$  obtained with the following diagnostics: [O II]  $\lambda 3726/\lambda 3729$ , [S II]  $\lambda 6731/\lambda 6716$  and [Cl III]  $\lambda 5538/\lambda 5518$ . For consistency, in the case of HH 204 we rely on the  $n_e$  derived from [Fe III] lines since values of  $10^4 - 10^6 \text{ cm}^{-3}$ , are above the critical densities of the CELs involved in the more common diagnostics. The simultaneous estimation of  $n_e$  ([Fe III]) and  $T_e$  ([Fe III]) in HH 204 is achieved by a maximum-likelihood procedure, as described in Paper I. However, in HH 204, we have confident detections of [Fe III]  $\lambda \lambda 3240, 3335$  lines from the  $^5D - ^3D$  transitions, which arise from higher levels than multiplets  $^5D - ^3F$  and  $^5D - ^3P$  that give origin to some of the strongest [Fe III] lines such as, for example,  $\lambda \lambda 4658.17, 4701.64, 4607.12, 4667.11$  and  $\lambda \lambda 5270.57, 5011.41$ , respectively. Thus, the ratios of the lines coming from the aforementioned multiplets are highly dependent on  $T_e$  as it is shown in Fig. 3. We include the following lines in the maximum-likelihood calculation: [Fe III]  $\lambda \lambda 3239.79, 3334.95, 4658.17, 4701.64, 4881.07, 4607.12, 4667.11, 5011.41, 5270.57$ . This collection of lines allows us to obtain well-constrained values of  $T_e$  ([Fe III]) and  $n_e$  ([Fe III]). The intensity ratios of these selected lines are consistent with the predicted ones when using transitions coming from the same atomic level (which are independent of the physical conditions of the gas), as we show in Table A6. Another density indicator that can be derived from our data is  $n_e(\text{O II})$ , but

only for the nebular component, which is the only one where we detect RLs of multiplet 1 of O II.

Once the representative  $n_e$  is adopted for each component, we estimate  $T_e$  through several diagnostics based on CELs as it is shown in Table 3. In the case of  $T_e$  ([S III]), telluric absorptions affect the line  $\lambda 9069$  in the nebular and Blue Layer components. Thus, we adopt  $I([\text{S III}] 9531)/I([\text{S III}] 9069) = 2.47$  ([Podobedova et al. 2009](#)) in these cases. In HH 204 we were able to measure the auroral [O I]  $\lambda 5577$  line free from sky emission contamination, which permitted us to estimate  $T_e$  ([O I]). In the Blue Layer, the estimations of  $T_e$  ([O II]) and  $T_e$  ([S II]) are affected by some extended residual emission of HH 204 in the auroral lines that crosses the cut border, affecting the first pixels of cut 2.  $T_e(\text{He I})$  was estimated using the average values obtained from  $I(\lambda 7281)/I(\lambda 6678)$ ,  $I(\lambda 7281)/I(\lambda 4922)$  and  $I(\lambda 7281)/I(\lambda 4388)$  He I line intensity ratios. Finally, we define  $T_e(\text{low})$  as the weighted average of  $T_e$  ([N II]),  $T_e$  ([O II]) and  $T_e$  ([S II]) while  $T_e(\text{high})$  is the weighted average of  $T_e$  ([O III]) and  $T_e$  ([S III]).

The resulting physical conditions for all the components are shown in Table 3.

### 4.2 Ionic abundances

We assume the values of  $n_e$  and the  $T_e$  indicator appropriated for each ion –assuming a three-zone approximation– to derive the ionic abundances of the different components. We use  $T_e(\text{low})$  for N<sup>+</sup>, O<sup>+</sup>, S<sup>+</sup>, Cl<sup>+</sup>, Ca<sup>2+</sup>, Cr<sup>+</sup>, Fe<sup>+</sup>, Fe<sup>2+</sup>, Ni<sup>+</sup> and Ni<sup>2+</sup> and  $T_e$  ([S III]) for S<sup>2+</sup> and Cl<sup>2+</sup>. In the case of Ne<sup>2+</sup>, O<sup>2+</sup> and Ar<sup>3+</sup>, we use  $T_e(\text{high})$ . For the nebular components, we derive the He<sup>+</sup>, C<sup>2+</sup> and Ar<sup>2+</sup> abundances using  $T_e(\text{high})$ , but  $T_e(\text{low})$  for HH 204, as we discuss in Sec. 5.1. For the abundance calculations, we follow the same methodology described in Paper I except in some particular cases that are discussed below together with ionic abundance determinations not considered in Paper I.

### 4.3 Ionic abundances of Fe and Ni

In HH 204, the emission lines of [Fe II], [Ni II], [Fe III] and [Ni III] are considerably enhanced in comparison with what is observed in the nebular components. We were able to observe weak lines of multiplets and transitions from these ions which allows us to explore their abundances in detail. Optical lines coming from the upper levels of the Fe<sup>+</sup> atom can be affected by continuum pumping ([Lucy 1995](#); [Rodríguez 1999](#); [Verner et al. 2000](#)). However, lower levels that produce the emission lines of multiplet  $a^4F - a^4P$  are mostly populated by collisions ([Baldwin et al. 1996](#)). One of the strongest lines of this multiplet, [Fe II]  $\lambda 8616.95$  ( $a^4F_{9/2} - a^4P_{5/2}$ ), could not be detected due to the instrumental gap of UVES in the red arm. However, weaker lines arising from the same upper level as  $\lambda \lambda 9051.95, 9399.04$  ( $a^4F_{7/2} - a^4P_{5/2}, a^4F_{5/2} - a^4P_{5/2}$ ), detected in HH 204, must be useful for the same purpose. Although the transition probabilities of the weakest detected lines coming from the  $a^4P_{1/2}, a^4P_{3/2}$  and  $a^4P_{5/2}$  levels should be revised (in addition to possible undetected telluric absorptions), there is a good agreement between the measured line ratios of [Fe II]  $9051.95/9399.04, 8891.93/9226.63$  and  $9267.56/9033.49$  and the theoretical predictions as it is shown in Table A7. In order to briefly test the chosen atomic data, we take advantage of the theoretical density dependence between the population of the  $a^4P_{1/2}$  and the  $a^4P_{5/2}$  levels as it is shown in Fig. 4. By using the estimated  $T_e(\text{low})$  for HH 204 and the [Fe II]  $\lambda 9268/\lambda 9052$  intensity ratio, we obtain

<sup>1</sup> The weights were defined as the inverse of the square of the error associated to each density diagnostic.



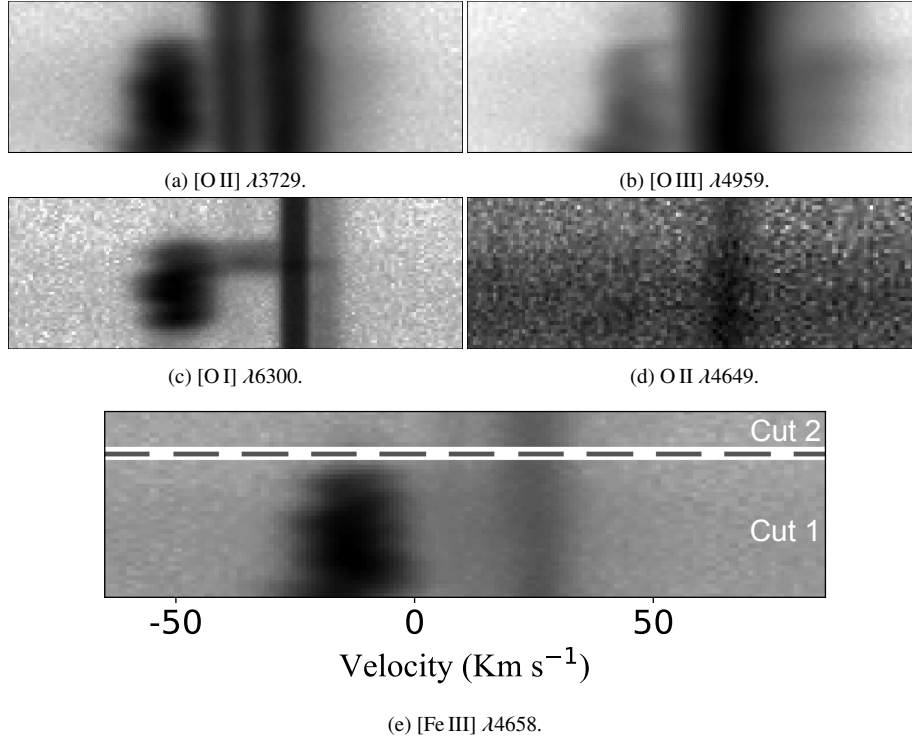


**Figure 2.** *Upper panels:* Sample of representative lines in the bi-dimensional spectrum. The Y axis corresponds to the spatial direction (up east, down west, see Fig. 1 for the spatial location of the slit) while the X axis is the spectral axis. All figures are centered at  $\lambda_0$ , the rest-frame reference wavelength of each line. The “ball-shaped” emission corresponds to HH 204. The slightly blue shifted component with respect to the nebular one is the “Blue Layer” (Deharveng 1973; García-Díaz & Henney 2007), mainly noticeable in the emission of low ionization ions such as [O II]. *Bottom panel:* Emission of the [Fe III]  $\lambda 4658.17$  line as well as the limits and extension of the different spatial cuts selected to analyse each velocity component. Cut 1 is at the bottom, which corresponds to the westernmost one. The spatial coverage is 7.38 arcsec and 1.97 arcsec for cuts 1 and 2, respectively. The velocity scale is heliocentric.

**Table 3.** Physical conditions determined from several diagnostics.

Diagnostic	Cut 1		Cut 2	
	HH 204	Nebula+Blue Layer	Blue Layer	Nebula
$n_e$ ( $\text{cm}^{-3}$ )				
[O II] $\lambda 3726/\lambda 3729$	$15420^{+7740}_{-3850}$	$1130^{+150}_{-110}$	$400^{+140}_{-120}$	$1480^{+190}_{-180}$
[S II] $\lambda 6731/\lambda 6716$	$11350^{+9920}_{-3890}$	$1350^{+290}_{-260}$	$300^{+140}_{-120}$	$1230^{+250}_{-230}$
[Cl III] $\lambda 5538/\lambda 5518$	$13370^{+1990}_{-1830}$	$1630^{+370}_{-320}$	-	$1930^{+720}_{-650}$
[Fe II] $\lambda 9268/\lambda 9052$	$13100^{+2860}_{-2990}$	-	-	-
[Fe III] $\lambda 4658/\lambda 4702$	$13040^{+3830}_{-3130}$	$3380^{+1810}_{-1340}$	-	$3200^{+2540}_{-1540}$
$n_e(\text{O II})$	-	$1350 \pm 150$	-	$1050 \pm 200$
[Fe III]*	$13540 \pm 1210$	-	-	-
<b>Adopted</b>	<b><math>13540 \pm 1210</math></b>	<b><math>1230 \pm 160</math></b>	<b><math>350 \pm 50</math></b>	<b><math>1440 \pm 170</math></b>
$T_e$ (K)				
$T_e$ (He I)	$8790^{+480}_{-430}$	9760:	5650:	7980:
[O I] $\lambda 5577/\lambda 6300+64$	$8290^{+430}_{-320}$	-	-	-
[N II] $\lambda 5755/\lambda 6584$	$8760^{+170}_{-180}$	$8530^{+150}_{-190}$	$8120^{+390}_{-360}$	$8440^{+170}_{-210}$
[O II] $\lambda \lambda 3726+29/\lambda \lambda 7319+20+30+31$	-	-	$10390^{+730}_{-640}$	$9120^{+430}_{-470}$
[S II] $\lambda \lambda 4069+76/\lambda \lambda 6716+31$	$8260^{+640}_{-500}$	$11470^{+950}_{-630}$	$10440^{+1360}_{-1030}$	$9890^{+650}_{-610}$
[O III] $\lambda 4363/\lambda \lambda 4959+5007$	$12430^{+180}_{-220}$	$8010^{+90}_{-80}$	-	$8120^{+90}_{-100}$
[S III] $\lambda 6312/\lambda \lambda 9069+9531$	$9310^{+220}_{-330}$	$8180^{+190}_{-230}$	$7710^{+510}_{-400}$	$8010^{+250}_{-210}$
[Fe III]*	$8210 \pm 220$	-	-	-
<b><math>T_e</math> (low) Adopted</b>	<b><math>8760 \pm 180</math></b>	<b><math>8530 \pm 190</math></b>	<b><math>8120 \pm 390</math></b>	<b><math>8440 \pm 210</math></b>
<b><math>T_e</math> (high) Adopted</b>	<b><math>12430 \pm 220</math></b>	<b><math>8030 \pm 60</math></b>	<b><math>7710 \pm 510</math></b>	<b><math>8110 \pm 90</math></b>

\* indicates that a maximum likelihood method was used.

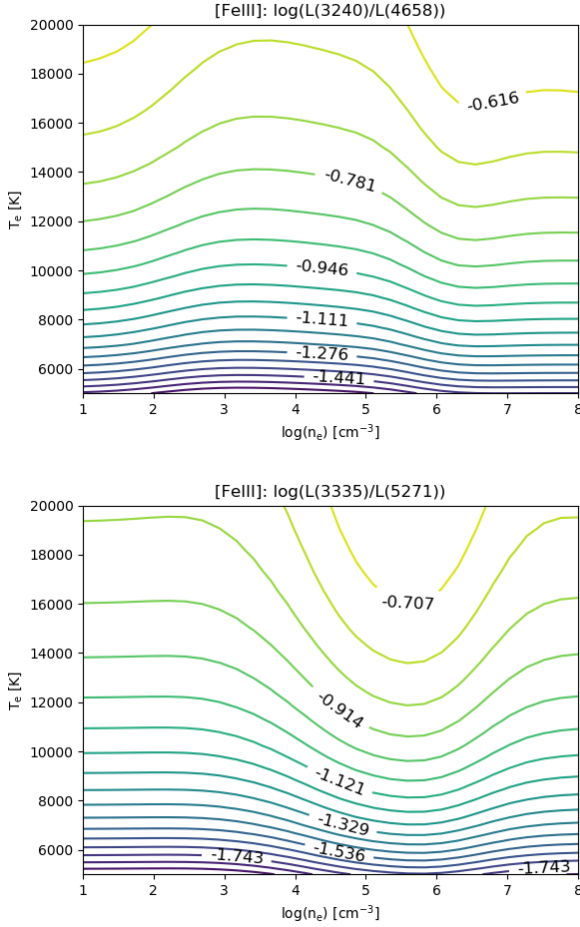


**Figure 3.** Predicted dependence of the [Fe III]  $\lambda 3240/\lambda 4658$  and  $\lambda 3335/\lambda 5271$  line intensity ratios with physical conditions.

$n_e([\text{Fe II}]) = 13100^{+2860}_{-2990} \text{ cm}^{-3}$ , which is consistent with the rest of density diagnostics shown in Table 3. In the Nebula+Blue Layer spectra from cut 1, [Fe II] lines are partially enhanced by the strong emission of HH 204. Since the [Fe II] lines in this component are rather weak, any small contribution from the tail of the HH 204 emission can significantly affect the  $\text{Fe}^+$  abundance. This is not a problem in cut 2, where the  $\text{Fe}^+$  abundance of the nebular component can be derived from the confident measurement of the [Fe II]  $\lambda 8891.93$  line.

Due to the low ionization degree of HH 204, we expect that  $\text{Fe}^+$  and  $\text{Ni}^+$  are important contributors to its total Fe and Ni abundances. Therefore, it seems pertinent to discuss in some detail the degree of confidence of the abundance determinations based on these two ions. The  $a^4\text{F} - a^4\text{P}_{5/2}$  transitions of [Fe II] and the  $a^2\text{D} - a^2\text{F}_{7/2}$  ones of [Ni II] have practically the same excitation energy, giving origin to lines close in wavelength (Bautista et al. 1996). However, there is an important difference between their sensitivity to fluorescence by continuum pumping due to the multiplicity of their ground states. Photoexcitations from the  $\text{Fe}^+ \text{ } ^6\text{D}$  ground state to the quartet levels have low probability and lines produced by intercombination transitions from sextet to quartet levels should be very weak (Bautista & Pradhan 1998). However, Rodríguez (1999) pointed out that the lowest quartet level,  $a^4\text{F}_{9/2}$ , may be metastable and promote excitations to higher quartet levels. The main pumping routes starting in this level were studied by Verner et al. (2000) at

densities above  $10^4 \text{ cm}^{-3}$ , finding that this pumping populates the levels  $a^4\text{H}$ ,  $b^4\text{F}$ ,  $b^4\text{P}$  and  $a^4\text{G}$ . Since transitions from any of these levels to  $a^4\text{P}$  are rather weak, it remains practically unaffected. Nevertheless, in the case of [Ni II], the ground state and the participating levels are doublets which make fluorescence effects by continuum pumping more probable (Bautista et al. 1996). However, an important factor that plays against the influence of fluorescence effects in [Ni II] in the case of HH 204 is its relatively large distance from  $\theta^1$  Ori C (150.4 arcsec), the main ionization source of the nebula and HH 204 (O’Dell et al. 2015, 2017b). In a simple procedure, following the formalism developed by Bautista et al. (1996, their equation 8), for a 3-level model (level 1:  $a^2\text{D}_{5/2}$ , level 2:  $a^2\text{F}_{7/2}$  and level 3:  $z^2\text{D}_{5/2}^0$ ), the critical densities  $n_{\text{cf}}$  – for which if  $n_e > n_{\text{cf}}$ , collisional excitations dominate over fluorescence – in two zones of the Orion Nebula (a and b), both excited by  $\theta^1$  Ori C, should be related as follows:

$$\frac{n_{\text{cf}, a}}{n_{\text{cf}, b}} = \left( \frac{J_{13, a}}{J_{13, b}} \right) \left( \frac{q_{12, b}}{q_{12, a}} \right), \quad (1)$$

where  $q_{12}$  is the Maxwellian averaged collisional strength for transitions from level 1 to 2 and  $J_{13}$  is the intensity of the continuum at energies of the  $1 \rightarrow 3$  transitions. If we choose the zone “a” as the one observed by Osterbrock et al. (1992) and the zone “b” as HH 204, we can assume  $q_{12, b}/q_{12, a} \approx 1$ , because the  $T_e$  determined by Osterbrock et al. (1992) and us are very similar (9000 K and 8760 K, respectively). On the other hand, by estimating the geometrical dilution of  $J_{13}$  in both areas (the zone observed by Osterbrock et al. (1992) is located at 63.98 arcsecs from  $\theta^1$  Ori C), we get a  $n_{\text{cf}, a}/n_{\text{cf}, b} \approx 5.53$ . By adopting the  $n_{\text{cf}, a}$  estimated by Bautista et al. (1996), we obtain  $n_{\text{cf}, b} \approx 2.17 \times 10^3 \text{ cm}^{-3}$ , which is rather small compared with the estimated density for HH 204 and therefore collisional excitation should dominate. Nevertheless, it must be considered that the apparently closer star  $\theta^2$  Ori A may be also a source of fluorescence for HH 204. However, by using the [Ni II]  $\lambda 7377.83$  ( $a^2\text{D}_{5/2} - a^2\text{F}_{7/2}$ ) line to obtain the  $\text{Ni}^+$  abundance and comparing with the  $\text{Fe}^+/\text{H}^+$  ratio, we obtain  $\log(\text{Ni}^+/\text{Fe}^+) = -1.27 \pm 0.06$ , in complete agreement with the solar value of  $\log(\text{Ni}/\text{Fe})_{\odot} = -1.25 \pm 0.05$  (Lodders 2019), indicating the absence of significant fluorescence effects (we expect larger fluorescence effects in  $\text{Ni}^+$ ). Therefore, we can discard the influence of  $\theta^2$  Ori A as a source of photon pumping of [Ni II] lines in HH 204. Since other [Ni II] lines, as  $\lambda 7411.61$  ( $^2\text{D}_{3/2} - ^2\text{F}_{5/2}$ ), give  $\text{Ni}^+$  abundances around a factor 2.20 higher, continuum pumping effects should be still important in the higher levels of the  $\text{Ni}^+$  atom in HH 204, although in a much lesser extent than in the area of the Orion Nebula observed by Osterbrock et al. (1992), where this factor reaches a value of 15.51 (Lucy 1995). Abundances of  $\text{Ni}^+$  in the rest of velocity components were not estimated since they require a more detailed analysis of the fluorescence conditions in the nebular gas, which goes beyond the scope of this paper.

We derive the  $\text{Fe}^{2+}$  abundance using the [Fe III] lines indicated in Sec. 4.1. It is noticeable the good agreement between  $T_e([\text{Fe III}])$ ,  $T_e([\text{O II}])$  and  $T_e([\text{S II}])$  in the case of HH 204, contrary to what was found in HH 529 II and HH 529 III, where  $T_e([\text{Fe III}])$  was more consistent with the temperature obtained for high ionization ions (Mendez Delgado & Amigos 2021). This is not surprising due to the different ionization degrees of HH 204 and HH 529 II+III (see Sec. 5).

In Paper I, we pointed out the inconsistency between the predicted and measured intensity ratios of [Ni III]  $^3\text{F} - ^3\text{P}_2$  transitions ( $\lambda 6533.76, 6000.16, 6946.39$ ) in HH 529 II, HH 529 III, HH 202 S

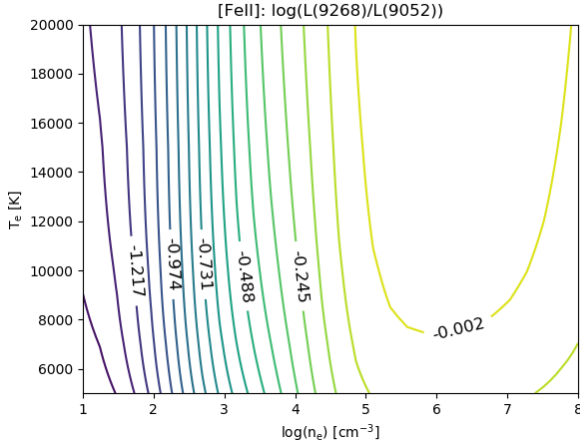


**Figure 4.** Predicted dependence of the [Fe II]  $\lambda 9268/\lambda 9052$  line intensity ratios with physical conditions.

and several zones of the Orion Nebula (see Table D11 of Paper I). We obtain a similar result for HH204,  $\lambda 6533.76/\lambda 6000.16 = 1.38 \pm 0.18$ , which is rather far from the predicted value of 2.19 value (Bautista 2001). We have a different situation for the intensity ratios of lines arising from the  $^1D_2$  level. After subtracting the small contribution of [Cl III]  $\lambda 8499.60$  to the measured intensity of [Ni III]  $\lambda 8499.62$ , we obtain  $\lambda 7889.93/\lambda 8499.62 = 2.65 \pm 0.19$  in agreement with the predicted value of 2.47 (Bautista 2001). This indicates that, with the atomic data available, the most confident determinations of the  $Ni^{2+}$  abundance can be obtained with these last lines. Thus, we will adopt the  $Ni^{2+}$  abundances determined from [Ni III]  $\lambda 7889.93$  line. However, this line is affected by a sky feature in the nebular components, using the  $Ni^{2+}$  abundance obtained with [Ni III]  $\lambda 6533.76$  in these cases.

#### 4.4 Ionic abundances based on RLs

For the nebular components,  $He^+$  abundances were derived using  $T_e(\text{high})$  and the lines considered in Table D14 of Paper I, which are the least affected ones by the meta-stability of the  $2^3S$  level. However, we have used  $T_e(\text{low})$  for HH 204. In this component, our determination of  $T_e(He\text{ I})$  is more consistent with  $T_e(\text{low})$ . This is because in HH 204, [O III] emission arises from a small localized area of higher ionized gas and  $T_e([O\text{ III}])$  is not representative of the  $He^+$  volume, as we describe in Sec. 5.1.

C II  $\lambda 4267$  is partially blended in the two velocity components of cut 1 and therefore we base our calculations on the intensity of C II  $\lambda 9903$ . We use C II  $\lambda 4267$  in cut 2.  $C^{2+}$  abundance estimations based on both lines are in complete agreement in cut 2. As in the case of the  $He^+$  abundance determinations, we consider  $T_e(\text{low})$  as representative of this ion in HH 204.

Contrary to the situation presented in Paper I, in HH 204, O I RLs from multiplet 1 are deeply affected by sky features with the exception of  $\lambda 7771.94$ . Based on the intensity of this line, we derive the  $O^+$  abundance of this HH object using the procedure described in Eq. 2 of Esteban et al. (1998) and the lines strengths from Wiese et al. (1996).

Estimations of the  $O^{2+}$  abundance were based on the available O II RLs from multiplet 1. In the case of HH 204, the estimation is based entirely in the intensity of  $\lambda 4649.13$  line, whose estimate is rather an upper limit to its real value.

#### 4.5 Ionic abundances of $Ca^+$ and $Cr^+$

We were able to measure some [Ca II] and [Cr II] lines with a good signal-to-noise ratio in HH 204. Thus, it permits us to estimate its  $Ca^+$  and  $Cr^+$  abundances. However, [Cr II] lines may be affected by fluorescence similarly to [Ni II] ones. The energies corresponding to  $a^2D - a^2F_{7/2}$  transitions of [Ni II] are similar to  $a^6S - a^6D$  ones of [Cr II]. Moreover, in both cases the lower – ground – and upper levels have the same multiplicity, so the excitation of the upper level by starlight is likely. Therefore, it seems reasonable to assume that if fluorescence effects are important for [Ni II] lines, they will also be important for [Cr II] lines. However, in HH 204, as we discuss in Sec. 4.3, collisional excitations dominate over fluorescence in the aforementioned [Ni II] transitions and this may be also the case for [Cr II]. With this assumption, we obtain an abundance ratio  $\log(Cr^+/H^+) = 4.28 \pm 0.03$ . By comparing this value with the  $Fe^+$  and  $Ni^+$  abundances, we obtain  $\log(Cr^+/Ni^+) = -0.61 \pm 0.05$  and  $\log(Cr^+/Fe^+) = -1.88 \pm 0.07$ , in agreement with the solar values of  $\log(Cr/Ni)_\odot = -0.57 \pm 0.05$  and  $\log(Cr/Fe)_\odot = -1.82 \pm 0.04$ , respectively (Lodders 2019). However, the spatial distribution of the  $Cr^+/Ni^+$  and  $Cr^+/Fe^+$  ratios along the HH 204 jet is not completely constant, as it is described in Sec. 5.2, which may be indicative of different ionization/depletion patterns between these elements. Unfortunately, due to the lack of atomic data, we can not derive the  $Cr^{2+}$  abundance, although several [Cr III] lines were detected.

In the case of the  $Ca^+$  abundance, we base our estimations in the [Ca II]  $\lambda 7323.89$  line since  $\lambda 7291.47$  is affected by a telluric absorptions in our observations. Due to its low ionization potential, smaller than that of hydrogen, and given the presence of an ionization front in HH 204 (Núñez-Díaz et al. 2012), the resulting abundance may not represent the real gaseous  $Ca^+$  abundance in the photoionized gas of HH 204.

### 5 UNVEILING HH 204

As it was mentioned in Sec. 3 we measure several lines pixel by pixel throughout the spatial coverage of HH 204. The spatial resolution in the blue and red arms of UVES is slightly different. Cut 1 include 30 pixels in the blue arm and 42 in the red one. In the pixel by pixel measurements, renormalization between lines in common in each arm is not enough to dilute possible differences in the integrated flux. However,  $H\beta$  is observed in the spectra of both arms and therefore we split our pixel-spectra in two parts, 27 blue-pixel-spectra and 37 red-pixel-spectra, both groups normalized with respect to  $f(H\beta)$ . The missing first pixels (from east to west) of cut 1 of both arms were not included since the emission of HH 204 was too faint. We proceeded as follows: based on the [Fe III]  $\lambda 4658.17/\lambda 4701.64$  line ratios we derive  $n_e$  along HH 204 in the blue arm. Once the distribution of density was estimated the estimation of  $T_e([O\text{ III}])$  was done, also in the blue arm through the [O III]  $\lambda 4363.21/\lambda 4958.91$  line ratio. The spatial distribution of  $n_e$  was linearly interpolated in the red arm to estimate  $T_e([S\text{ III}])$  and  $T_e([N\text{ II}])$ . Once the physical conditions are determined, we estimate the ionic abundances using the same procedure followed in Sec. 4.2. The zero point of the spatial distribution is located at coordinates: RA(J2000)=05<sup>h</sup>35<sup>m</sup>22<sup>s</sup>.63, DEC(J2000)=−05°25′21.86″, just at the apparent eastern – external – edge of the bowshock. To estimate the distance from the bowshock along the jet, we adopt an heliocentric distance of  $410 \pm 10$  pc (Binder & Povich 2018) to the Orion Nebula, based on *Gaia* DR2 parallaxes (Gaia Collaboration et al. 2018).

**Table 4.** Chemical abundances obtained with CEL's of the integrated spectra of each component.

Ion	HH 204	Cut 1	Cut 2	
		Nebula+Blue Layer	Blue Layer	Nebula
O <sup>+</sup>	8.62 ± 0.05	8.14 ± 0.05	8.26 <sup>+0.13</sup> <sub>-0.09</sub>	8.18 <sup>+0.06</sup> <sub>-0.05</sub>
O <sup>2+</sup>	6.34 ± 0.02	7.96 ± 0.02	7.33 <sup>+0.15</sup> <sub>-0.10</sub>	8.04 ± 0.02
N <sup>+</sup>	7.72 ± 0.03	7.34 ± 0.03	7.40 <sup>+0.08</sup> <sub>-0.06</sub>	7.29 <sup>+0.04</sup> <sub>-0.03</sub>
Ne <sup>2+</sup>	5.05 ± 0.03	7.16 ± 0.02	-	7.23 <sup>+0.03</sup> <sub>-0.02</sub>
S <sup>+</sup>	6.60 ± 0.04	5.93 ± 0.03	5.92 <sup>+0.07</sup> <sub>-0.06</sub>	5.86 <sup>+0.04</sup> <sub>-0.03</sub>
S <sup>2+</sup>	6.80 ± 0.03	6.84 ± 0.03	6.85 <sup>+0.10</sup> <sub>-0.08</sub>	6.89 ± 0.04
Cl <sup>+</sup>	4.72 ± 0.03	4.17 ± 0.03	4.08 <sup>+0.10</sup> <sub>-0.09</sub>	4.05 ± 0.04
Cl <sup>2+</sup>	4.77 <sup>+0.04</sup> <sub>-0.03</sub>	4.93 ± 0.04	4.99 <sup>+0.16</sup> <sub>-0.12</sub>	4.98 <sup>+0.06</sup> <sub>-0.05</sub>
Ar <sup>2+</sup>	5.66 ± 0.03	6.10 ± 0.02	5.99 <sup>+0.10</sup> <sub>-0.08</sub>	6.12 ± 0.02
Ar <sup>3+</sup>	-	3.64 <sup>+0.13</sup> <sub>-0.12</sub>	-	-
Fe <sup>+</sup>	6.16 ± 0.04	-	-	4.72 ± 0.08
Fe <sup>2+</sup>	6.49 ± 0.02	5.72 ± 0.04	5.56 <sup>+0.10</sup> <sub>-0.08</sub>	5.77 ± 0.04
Fe <sup>3+</sup>	<5.11	5.73 ± 0.13	-	-
Ni <sup>+</sup>	4.89 ± 0.02	-	-	-
Ni <sup>2+</sup>	5.13 ± 0.03	4.37 ± 0.09	-	-
Ca <sup>+</sup>	3.50 ± 0.03	-	-	-
Cr <sup>+</sup>	4.28 ± 0.03	-	-	-

**Table 5.** Chemical abundances obtained with RL's of the integrated spectra of each component.

Ion	HH 204	Cut 1	Cut 2	
		Nebula+Blue Layer	Blue Layer	Nebula
He <sup>+</sup>	10.53 ± 0.02	10.85 ± 0.03	10.66 ± 0.06	10.92 ± 0.04
O <sup>+</sup>	8.57 ± 0.03	-	-	-
O <sup>2+</sup>	< 7.54	8.25 ± 0.06	-	8.40 ± 0.03
C <sup>2+</sup>	7.76 ± 0.07	8.22 ± 0.04	-	8.37 ± 0.02

### 5.1 Small scale physical conditions

The resulting physical conditions are shown in Fig. 5. We can see that  $n_e([\text{Fe III}])$  increases as one approaches the shock front up to a factor of about 2, compared to the values at  $\sim 13$  mpc from the bowshock. The estimated  $T_e([\text{N II}])$  is practically isothermal while  $T_e([\text{S III}])$  increases slightly as we move away from the bowshock towards  $\theta^1$  Ori C. On the other hand,  $T_e([\text{O III}])$  strongly increases as approaching the bowshock.

The interpretation of the spatial distribution of  $T_e([\text{O III}])$  is complex. In the presence of a shock, a photoionized gas can be heated at a temperature higher than that fixed by the photoionization equilibrium (Zel'dovich & Raizer 1967) (see Sec. 11 of Paper I). After the shock passage, the gas cools down by radiative emission until reaching equilibrium temperature, forming a cooling zone whose extension will be inversely proportional to the electron density (say reference). If we assume that the high- $T_e([\text{O III}])$  area corresponds to the cooling zone formed after the shock, the fact that  $T_e([\text{S III}])$  and  $T_e([\text{N II}])$  are not affected in the same way, would imply that the high-ionization degree gas has a much lower density than the one of low and medium-ionization degree and that both components coexist in HH 204. Although there is evidence of entrainment of material emitting in [O III] CELs feeding HH 204 (Doi et al. 2004; García-Díaz & Henney 2007), panels (a) and (b) from Fig. 2 show that the spatial and spectral distribution of [O III] and [O II] do not differ considerably. This fact indicates that there is no gas with two different physical conditions or, on the contrary, both components are intertwined in such a way that our observations cannot separate them.

On the other hand, the kinetic energy of the electrons moving at a velocity  $\sim 100 \text{ km s}^{-1}$  relative to the rest frame is  $\sim 51.8 \text{ eV}$  which is able to ionize an O<sup>+</sup> ion at rest into O<sup>2+</sup> and excite it to its higher levels. In the bowshock, the difference in velocity between the “target” and the “projectile” gas is maximum, and so it would be the shock-ionization and excitation rates to the <sup>1</sup>S<sub>0</sub> level of O<sup>2+</sup>. This would create a “high temperature”- $T_e([\text{O III}])$  that would decrease as we move away from the bowshock.

The spatial distribution of the intensity of [O III]  $\lambda\lambda$  4363, 4959 lines is presented in Fig. 6. We can see that the intensities of both lines fall simultaneously when approaching the bowshock from the farthest point included in the diagram (from  $\sim 12.7$  mpc away), so their ratio remains constant. This is consistent with a drop in the ionization parameter  $U$ , on which the degree of ionization of the photoionized gas depends and is proportional to  $r^{-2} \cdot n_e^{-1}$ , where  $r$  is the distance to the ionizing source. The fall is consistent with a departure from  $\theta^1$  Ori C and the increase in density as we approach the bowshock. At distances from the bowshock less than  $\sim 4.9$  mpc, the intensity of both lines increases, but more strongly in the case of [O III]  $\lambda$ 4363 line, increasing  $T_e([\text{O III}])$ . This can be explained by the aforementioned combination of shock-ionization and excitation process that would increase  $n(\text{O}^{2+})$  and the population of its upper levels. Note, that given the drop in  $U$  at the bowshock, there would not be enough ionizing photons to maintain the photoionization equilibrium in the emission of [O III] CELs. All these considerations imply that  $T_e([\text{O III}])$  should not be used as a representative of the gas at distances close to the bowshock for abundance determinations.

Although part of the aforementioned high-ionization degree

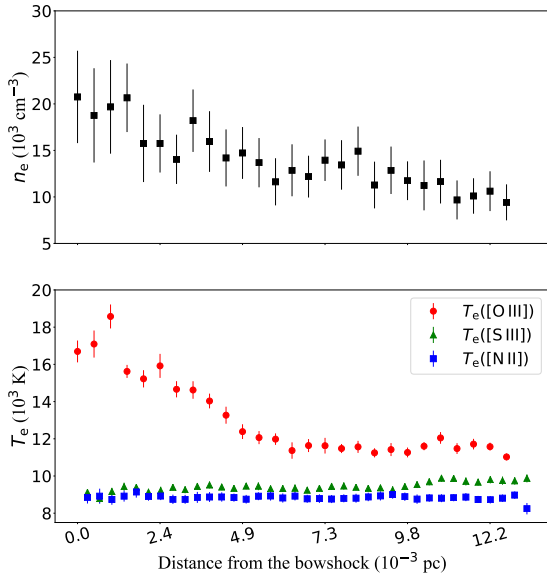


**Figure 5.** Spatial distribution of physical conditions as a function of the distance to the eastern – external – edge of the bowshock of HH 204. *Upper panel:*  $n_e$  ([Fe III]). The gas compresses as it approaches the shock front, increasing its density. *Bottom panel:*  $T_e$  estimates with 3 diagnostics. While  $T_e$  ([S III]) and  $T_e$  ([N II]) remain unaltered,  $T_e$  ([O III]) shows a strong increase when approaching the shock.

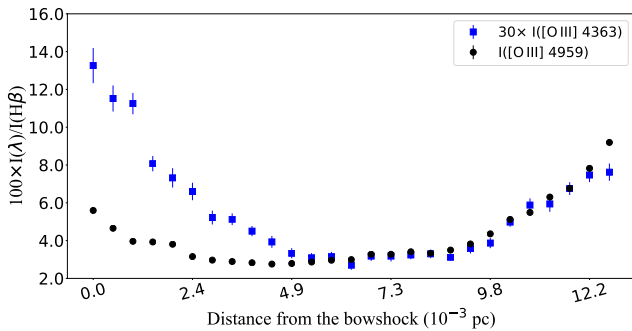


**Figure 6.** Same as Fig. 5 for the intensities of the [O III]  $\lambda\lambda 4363, 4959$  lines. Line intensity ratios with respect to  $H(\beta)$  have been normalized for a more clear comparison.

gas may be out of photoionization equilibrium, its impact is negligible in the global abundance analysis of HH 204. Considering the ionization fraction  $O^{2+}/(O^+ + O^{2+}) = 0.005 \pm 0.001$  (see Table 4) – which would increase to  $O^{2+}/(O^+ + O^{2+}) = 0.017 \pm 0.003$  if we determine the  $O^{2+}$  abundance by using  $T_e$  ([N II]) – we infer that the contribution of the  $O^{2+}$  from the high-ionization degree gas is around  $\sim 1\%$  of the oxygen abundance. A similar result is found for other metals. For example, by considering the solar Ne/O ratio recommended by Lodders (2019) and the  $Ne^{2+}/O$  value of HH 204, we estimate that  $Ne^{2+}/Ne \sim 0.001$ . The fact that  $T_e$  ([N II]) and  $T_e$  ([S III]) are kept in balance in HH 204 along the observed pixels proves that the low and medium-ionization degree gas, which comprises more than  $\sim 99\%$  of the total, is in photoionization equilibrium.

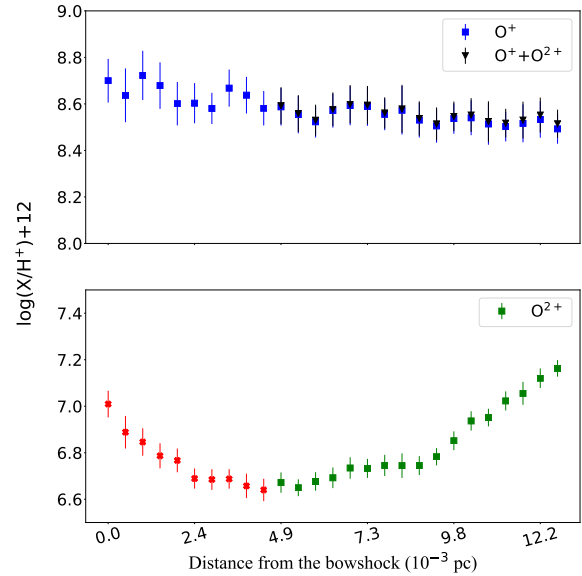


**Figure 7.** Same as Fig. 5 for ionic and total abundances of O. *Upper panel:*  $O^+$  and total O abundances. The total abundance of O was calculated as the sum of  $O^+$  and  $O^{2+}$  in the area where  $T_e$  ([O III]) remains constant – distances between 4.9 and 13 mpc from the bowshock –. The contribution of  $O^{2+}$  to total O abundance is negligible compared to the abundance of  $O^+$ . *Bottom panel:*  $O^{2+}$  abundances. The red crosses show the zone clearly affected by the shock (see Fig. 5, Fig. 6 and Sec. 5.1). The green squares indicate the area where  $T_e$  ([O III]) remains constant.

## 5.2 Small-scale patterns in the ionic abundances

Fig. 7 shows the spatial distribution of the ionic abundances of O. As described in Sec. 5.1, the increase of  $T_e$  ([O III]) may be related to a contribution of collisional ionizations of  $O^+$  to  $O^{2+}$ . Therefore, we highlighted in red the  $O^{2+}$  abundances in this area in the bottom panel of Fig. 7. In the upper panel, we show the  $O^+$  abundances along all the distances range and the O ones in the area where  $T_e$  ([O III]) remains constant. This panel shows that practically all O is in  $O^+$  form. It should be noted that the collisional ionization of less than 1% of the  $O^+$  into  $O^{2+}$  would represent a factor  $\sim 2$  increase of  $O^{2+}$  abundance, while this would be well below the associated uncertainties of the  $O^+/H^+$  ratio and, therefore, it would be undetected.

In tables 4 and 5 we can see that the  $O^+$  abundances determined from CELs and RLs are consistent in HH 204, so we do not find an abundance discrepancy (AD) for this ion, contrary to the situation found in practically all photoionized nebulae. Fig. 8 indicates the absence of any significant AD in all the observed areas of HH 204, although some fluctuations can be present, they are very small in any case. The origin of the AD problem has been related with temperature, density or chemical inhomogeneities in the nebulae or fluorescence effects on the intensity of RLs. In relation to this, there are three properties of HH 204 that we want to highlight: (i) In Sec. 5.1, we show that the spatial distribution of  $T_e$  ([N II]) is constant, i. e. there are no significant temperature fluctuations in the plane of the sky that may be translated into fluctuations in the line of sight. The presence of temperature fluctuations would produce the underestimation of the  $O^+$  abundance based on CELs. (ii) In Sec. 4.3 we show that the effects of starlight fluorescence are



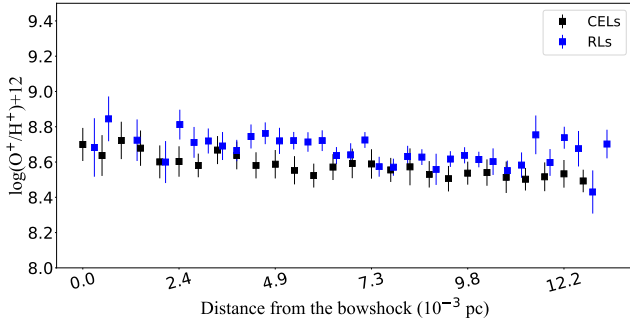


**Figure 8.** Same as Fig. 5 for  $O^+$  abundances determined with CELs and RLS.

negligible in the determination of the abundances of  $Ni^+$  and  $Fe^+$  due to the large distance between HH 204 and the ionizing source in addition to its high density. Thus, if there is any mechanism in which the continuum pumping can affect the population of the levels of multiplet 1 of OI, this may be diminished in a similar way. Moreover, (Mesa-Delgado et al. 2009) report an  $ADF(O^+) \sim 0$  in HH 202 S, which is located closer to the ionization source of the nebula, indicating that, in any case, OI lines of multiplet 1 are not likely to be exposed to fluorescence effects due to continuum pumping. (iii) The jet-geometry of HH 204, with an angle of  $\sim 27^\circ$  with respect to the plane of the sky (Henney et al. 2007), implies that the volume of gas integrated along the line of sight is relatively small, compared to the case of a jet flowing directly towards the observer or to observations of the Orion Nebula. Therefore, the existence of chemical or density inhomogeneities in the line of sight are unlikely. These three observational properties do not favor the presence of  $AD(O^+)$  in HH 204.

In Fig. 9 we present the ionic abundances of Cl and S. The species of the same degree of ionization present similar patterns in both elements. The variations of  $S^{2+}/H^+$  and  $Cl^{2+}/H^+$  ratios along HH 204 are rather small in comparison to  $S^+/H^+$  and  $Cl^+/H^+$  that show a decrease of 0.8 dex along the diagram with respect to the values close to the bowshock. At distances  $\lesssim 4.9$  mpc with respect to the bowshock, the abundances of  $S^+$  and  $Cl^+$  seem to stabilize and presumably, almost all S and Cl must be only once and twice ionized.

The distributions of the ionic abundances of Fe and Ni are clearly correlated as is shown in Fig. 10. Similar to the situation presented in Fig. 9 for S and Cl, close to the bowshock, the contribution of species more ionized than  $Fe^{2+}$  and  $Ni^{2+}$  to the total abundances should be negligible. The ratios of the ionic abundances between both elements remain constant as is shown in Fig 11, being  $\log(Fe^+/Ni^+) = 1.26 \pm 0.03$ ,  $\log(Fe^{2+}/Ni^{2+}) = 1.37 \pm 0.03$  and  $\log(Fe/Ni) = 1.33 \pm 0.03$ . Although the value of  $\log(Fe^{2+}/Ni^{2+})$  is slightly above the recommended solar value ( $\log(Fe/Ni)_\odot = 1.25 \pm 0.05$  (Lodders 2019)), this may be the consequence of a slight systematic underestimation of  $Ni^{2+}$  because, as we discussed in Sec. 4.3, the atomic data for this ion show some inaccuracies.

In Fig. 12 we show the similar spatial distributions of the abundances of  $He^+$  and  $Ar^{2+}$ . The abundances of these ions decrease as we approach the bowshock due to the decrease of the ionization degree as  $n_e$  increases. However, a small peak is observed at distances less than  $\sim 2.4$  mpc, probably due to the contribution of collisional ionization as discussed in Sec. 5.1 in the case of [O III] lines. However, the impact of this contribution of collisional ionization seems to be lower for these ions. For example, the fact that  $T_e(He I)$  is

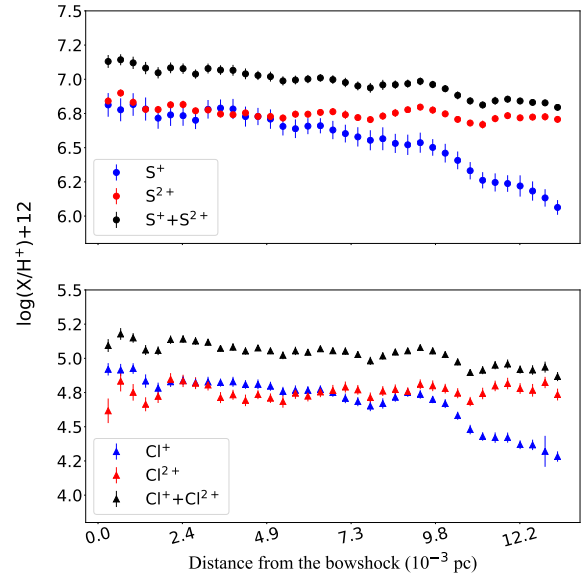


**Figure 9.** Same as Fig. 5 for ionic abundances of S (upper panel) and Cl (bottom panel).

consistent with  $T_e([N II])$  (see Sec. 4.1) reflects that the population of the singlet levels, which are used for the  $T_e(He I)$  determination, are largely unaffected.

In Fig. 13, we show that the abundance of  $N^+$  increases as we move towards the bowshock from values of  $7.53 \pm 0.03$ , until it stabilizes around  $7.75 \pm 0.02$ . At this point, all the nitrogen should be only once ionized. Figures 14 and 15 show the spatial distributions of  $Cr^+$  and  $Ca^+$  abundances, respectively. They are somewhat different to the ones of  $Fe^+$  or  $Ni^+$  (Fig. 10). This makes the  $Fe^+/Cr^+$  or  $Fe^+/Ca^+$  abundance ratios not constant, contrary to what is obtained for  $Fe^+/Ni^+$  (Fig. 16). In the case of the  $Fe^+/Cr^+$  ratio, the observed trend may be related to the slight differences between their ionization energies or to different depletion patterns. The curve defined by the  $Fe^+/Ca^+$  abundance ratio, may be due to the coexistence of this ion and  $H^0$  in the ionization front.

### 5.3 A direct measurement of $t^2$

Several works have studied the possible temperature inhomogeneities of the Orion Nebula on the plane of the sky (O'Dell et al. 2003; Mesa-Delgado et al. 2008; García-Díaz et al. 2008). However, the values of the Peimbert's  $t^2$  (Peimbert 1967) estimated in this way may differ substantially from the representative values of the gas integrated into the line of sight. Nevertheless, this is not a problem in the case of HH 204. Its jet geometry, propagating at an angle of  $\sim 27^\circ$  with respect to the plane of the sky (Henney et al. 2007), implies that the integrated volume in the line of sight is relatively small. If we assume a geometry of an elliptical paraboloid with the UVES slit located in the projection of the symmetry axis in the sky plane (see Fig. 1), then each pixel will integrate the emission of a representative zone of a disk of gas. Variations in the physical conditions would be expected mostly from disk to disk, being less likely in the azimuthal direction within each disk. As discussed in Sec. 5.1,  $T_e([O III])$  shows strong temperature variations along the observed area of HH 204. Since we know the small-scale

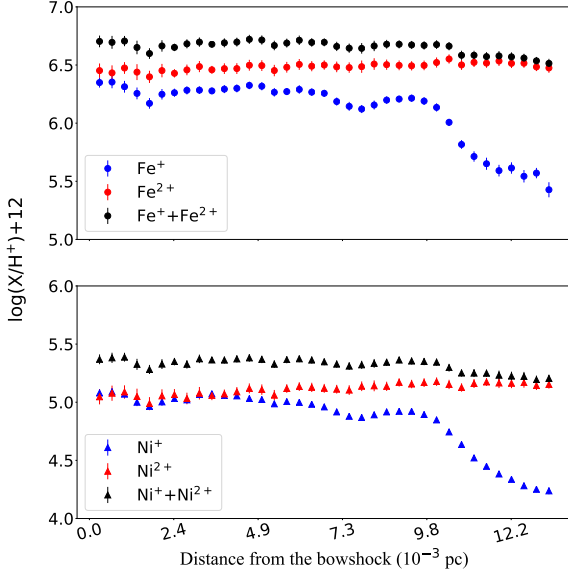


**Figure 10.** Same as Fig. 5 for ionic abundances of Fe (upper panel) and Ni (bottom panel).

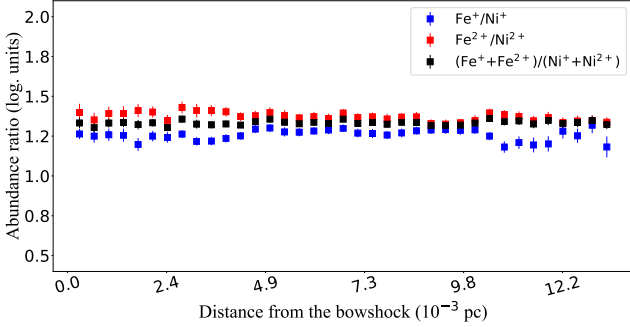


**Figure 11.** Same as Fig. 5 for the ratios of ionic abundances of Fe and Ni.

distribution of the physical conditions and the  $O^{2+}/H^+$  ratio determined using  $T_e([O III])$  along the jet, we can apply the formalism developed by Peimbert (1967) for estimating  $t^2(O^{2+})$  and  $T_0(O^{2+})$  directly from the definition. Eq. 9 and Eq. 12 from Peimbert (1967), are solved below, by assuming the aforementioned geometry:

$$T_0 = \frac{\int T_e n_e n(O^{2+}) dV}{\int n_e n(O^{2+}) dV} \approx \frac{\sum_{l=0}^{l=d} T_e n_e n(O^{2+}) l \Delta l}{\sum_{l=0}^{l=d} n_e n(O^{2+}) l \Delta l}, \quad (2)$$

$$t^2 = \frac{\int (T_e - T_0)^2 n_e n(O^{2+}) dV}{T_0^2 \int n_e n(O^{2+}) dV} \approx \frac{\sum_{l=0}^{l=d} (T_e - T_0)^2 n_e n(O^{2+}) l \Delta l}{T_0^2 \sum_{l=0}^{l=d} n_e n(O^{2+}) l \Delta l}, \quad (3)$$

where  $l$  is the distance variable along the jet and  $d$  is  $\sim 13$  mpc, the maximum observed distance. The amplitude of the curvature of the bowshock and the angle of the jet with the plane of the sky are canceled out. The results are  $T_0(O^{2+}) = 12060 \pm 80$  and  $t^2(O^{2+}) = 0.012 \pm 0.002$ . This is probably the first direct measurement of  $t^2$ , representative for the integrated gas volume. By testing

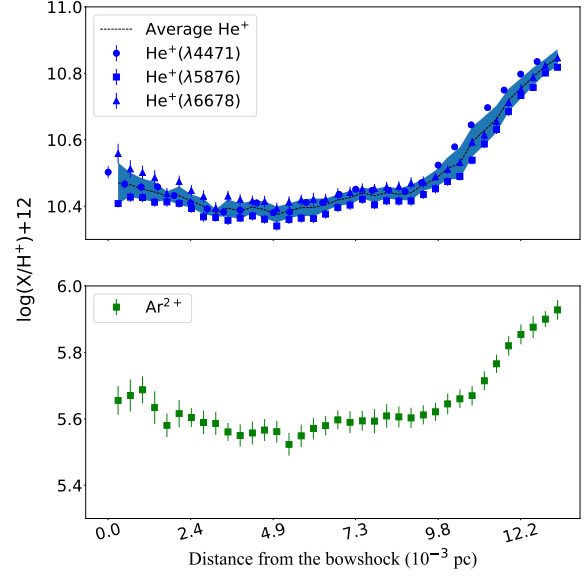


**Figure 12.** Same as Fig. 5 for  $He^+$  abundances (upper panel) and  $Ar^{2+}$  abundances (bottom panel).

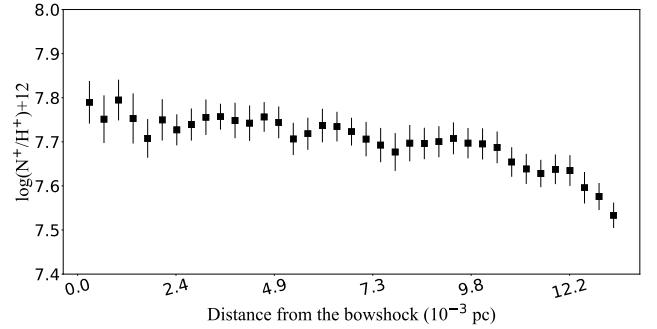


**Figure 13.** Same as Fig. 5 for  $N^+$  abundances.

the results with the Eq. 15 from Peimbert (1967), we obtain, that the expected measurement of  $T_e([O III])$  in the spectrum that results from adding all the pixels considered in this small-scale analysis is  $T_e([O III]) = 12690 \pm 100$ , in agreement with the results of Sec. 4.1 (see Table 3), validating our assumptions. Therefore, in our case, the temperature variations of the order of  $10^3$  K do not break the validity of approximating the temperature-dependence of the emissivity of the CELs through the first terms of a Taylor series, and can be properly characterized with the Peimbert's formalism.

#### 5.4 Deuterium lines in HH 204

### 6 TOTAL ABUNDANCES

In the case of the nebular components and the Blue Layer, total abundance of O, Cl, and S were estimated by adding the abundances of all their observed ions. Although there may be some contribution of  $S^{3+}$  and  $Cl^{3+}$ , the ionization correction factors (ICFs) of Stasińska (1978) and Esteban et al. (2015), respectively, predict negligible amounts of those species. In the case of N, Ne, Ar and C, we

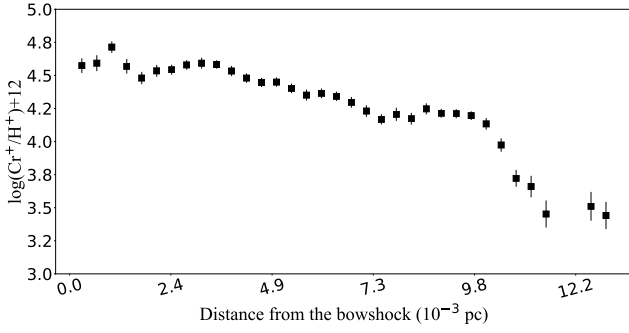


Figure 14. Same as Fig. 5 for  $\text{Cr}^+$  abundances.

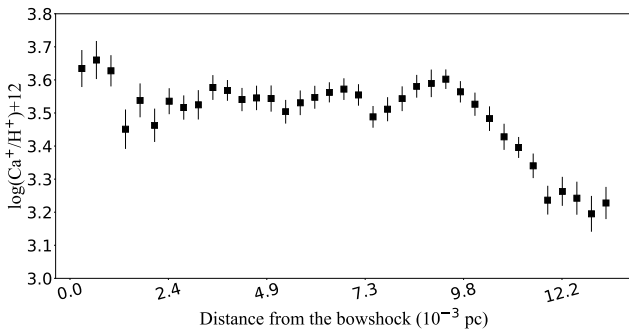


Figure 15. Same as Fig. 5 for  $\text{Ca}^+$  abundances.

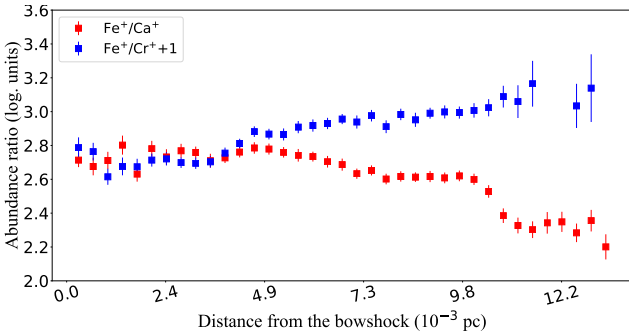


Figure 16. Same as Fig. 5 for  $\text{Fe}^+/\text{Ca}^+$  and  $\text{Fe}^+/\text{Cr}^+$  abundance ratios.

adopt the same ICFs used by Arellano-Córdova et al. (2020b). For Fe, we use the two ICFs proposed by Rodríguez & Rubin (2005). Since the real value of Fe should be between the predictions of both ICFs (Rodríguez & Rubin 2005), in Table 6 we present the two determinations as lower and upper limits of the Fe abundance.

In the case of HH 204, based on the results of Sec. 5, we decided not to derive total abundances of elements for which we only observe highly ionized ions such as He, Ne, Ar and C. In the cases of O, N, Cl, S, Fe and Ni, we can determine their total abundances without ICFs. As seen in Sec. 5, the spatial distribution of the abundances of the once and twice ionized ions of Cl, S, Fe and Ni tend to a constant value at distances close to the bowshock, where the degree of ionization becomes very low. In this zone, the contribution of three – or more – times ionized ions of these elements should be negligible. A similar situation occurs with N, where the contribution of  $\text{N}^{2+}$  becomes negligible close to the bowshock. Therefore, in Table 6 we present the total abundance values obtained by adding the mean abundances of the once and twice ionized ions of Cl, S,

Fe and Ni for distances less than 4.9 mpc from the bowshock. In the case of O and N, we only consider the abundance of once ionized ions in the same range of distances. At these distances, the spatial distribution of the  $\text{O}^+$  abundance determined from RLs is rather noisy as is shown in Fig. 8. This is because  $\text{OI } \lambda 7771.94$  line is very weak for the pixel-by-pixel analysis. In this case, we use the  $\text{O}^+$  abundance from RLs obtained from the integrated spectrum given in Table 4 and assume it for the total O abundance based on RLs.

## 7 THE EFFECTS OF LOWERING THE SPATIAL AND SPECTRAL RESOLUTION

In Sec. 5, we have carried out a pixel-by-pixel analysis of the physical conditions and ionic abundances of the ionized gas in HH 204, separating the different kinematical components. Now we are going to perform a similar analysis simulating a spectrum with lower spatial and spectral resolution, i.e. integrating the emission of all the components along the whole UVES slit. Contrary to the case studied in Paper I, where the components of HH 529 II and HH 529 III HH objects are fainter than the emission of the Orion Nebula, HH 204 is a quite brighter object, with an intensity similar to that of the other two components together. Therefore, the contribution of HH 204 to the integrated low-spectral resolution spectrum is important. Thus, we define a new spectrum by adding the flux of all the velocity components, which includes the emission of HH 204, the Blue Layer and the nebular emission of the Orion Nebula, along the entire UVES slit. Then we followed the procedure described in Sec. 3 for the reddening correction, obtaining  $c(\text{H}\beta) = 0.36 \pm 0.02$ .

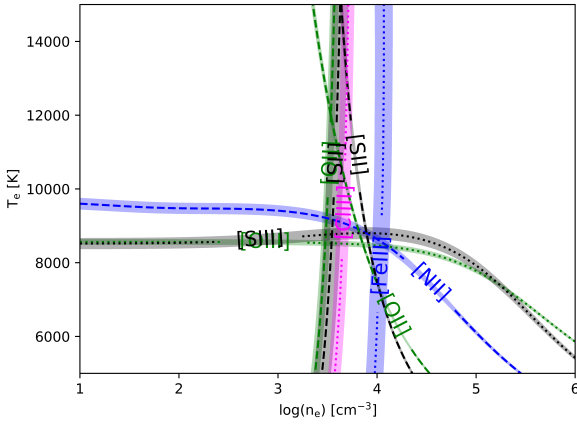
In Fig. 17, we present the resulting plasma diagnostics of the low-resolution spectrum. This diagram can be compared with those of the individual components, shown in Fig. A1. If we only had the information provided by this degraded spectrum, and apply the classic procedure of averaging  $n_e([\text{O II}])$ ,  $n_e([\text{S II}])$  and  $n_e([\text{Cl III}])$ , excluding any information provided by  $n_e([\text{Fe III}])$ , since the discrepancy of this diagnostic is generally interpreted as the effect of incorrect atomic data. Then we would obtain  $n_e = 3430 \pm 580$ . By using this value of density, we would calculate  $T_e([\text{O II}]) = 12140^{+950}_{-930}$ ,  $T_e([\text{S II}]) = 19220^{+9020}_{-2530}$ ,  $T_e([\text{N II}]) = 9200 \pm 200$ ,  $T_e([\text{S III}]) = 8740^{+230}_{-200}$  and  $T_e([\text{O III}]) = 8530^{+100}_{-120}$ . It must be noted that the resulting  $T_e([\text{N II}])$  is higher than the ones obtained for each individual component analyzed in Sec. 4.1. Moreover,  $T_e([\text{O II}])$  and  $T_e([\text{S II}])$ , the most density-dependent diagnostics, show very high values. However, their effect on abundance determinations could be somehow mitigated, as their associated uncertainties are very high and the use of a weighted mean of temperatures would reduce their contribution.  $T_e([\text{N II}])$  has always much lower uncertainties and is generally used as the preferred temperature diagnosis for low-ionization degree ions.

Based on the physical conditions obtained with this classical procedure, we can derive ionic abundances. For oxygen, using  $T_e([\text{N II}])$  as the representative temperature of the  $\text{O}^+$  and  $T_e([\text{O III}])$  for  $\text{O}^{2+}$ , we obtain:  $\text{O}^+ = 8.15 \pm 0.04$  and  $\text{O}^{2+} = 7.63 \pm 0.02$ . This implies  $\text{O} = 8.26 \pm 0.03$ . This value is smaller than the one determined for all the individual components. The only exception could be the Blue Layer in cut 2, which shows  $\text{O} = 8.31 \pm 0.12$  (See Table 6), whose uncertainty is large enough to encompass the value obtained for the low resolution spectrum. However, this does not mean the Blue Layer dominates the observed abundance of O, since it is the weakest component. This is exemplified in Fig. 18, which shows the line profile of  $f([\text{O II}] \lambda 3727)$ , one of the most intense lines emitted by the Blue Layer.

**Table 6.** Total abundances.

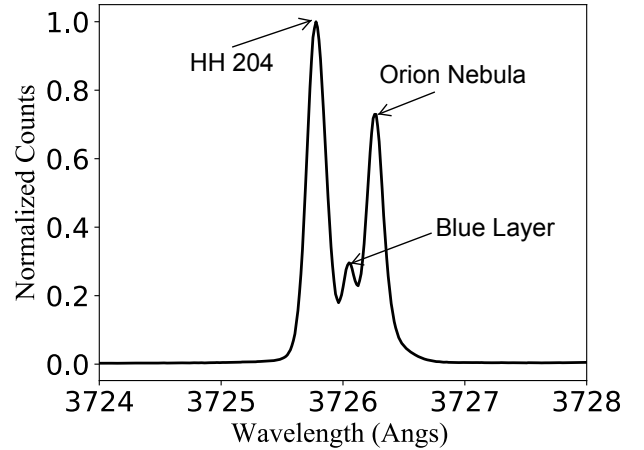
Element	HH 204	Cut 1	Cut 2	
		Nebula+Blue Layer	Blue Layer	Nebula
O	$8.62 \pm 0.05$	$8.36 \pm 0.03$	$8.31 \pm 0.12$	$8.42 \pm 0.04$
O*	$8.57 \pm 0.03$	-	-	-
N	$7.75 \pm 0.02$	$7.56^{+0.04}_{-0.03}$	$7.45^{+0.09}_{-0.08}$	$7.53 \pm 0.05$
Ne	-	$7.56 \pm 0.04$	-	$7.61 \pm 0.05$
S	$7.07 \pm 0.03$	$6.90 \pm 0.03$	$6.90 \pm 0.09$	$6.94 \pm 0.04$
Cl	$5.10 \pm 0.04$	$5.00 \pm 0.03$	$5.04 \pm 0.14$	$5.03 \pm 0.05$
Ar	-	$6.14 \pm 0.02$	$6.09 \pm 0.10$	$6.17 \pm 0.02$
Fe	$6.67 \pm 0.03$	$5.91-6.09$	$5.64-6.19$	$5.97-6.13$
Ni	$5.35 \pm 0.03$	-	-	-
C*	-	$8.49 \pm 0.05$	-	$8.64 \pm 0.04$

\* Based on RLs.

**Figure 17.** Plasma diagnostics of the spectrum defined by adding all the observed velocity components along the whole UVES slit.

The explanation of the low O abundance in the low resolution spectrum is due to using the classical procedure in estimating  $n_e$ . The classical density diagnostics are not capable of properly account for the high density of HH 204. Their sensitivity at  $n_e \sim 10^4 \text{ cm}^{-3}$  is much lower than for the normal range of values for H II regions,  $n_e \sim 10^2 - 10^3 \text{ cm}^{-3}$ , being their critical densities below the density of HH 204 (see Table D5 of Paper I). On the other hand,  $I([\text{Fe III}] \lambda 4658)/I([\text{Fe III}] \lambda 4702)$  is practically insensitive at densities smaller than  $n_e \sim 10^3 \text{ cm}^{-3}$ , and the critical density of this diagnostic is above  $\sim 10^6 \text{ cm}^{-3}$ . This property makes it a good indicator of the presence of high-density gas. In our case, the  $n_e([\text{Fe III}]) = 10790^{+3230}_{-2620}$  we obtain for the low resolution spectrum is rather close to the density of HH 204. This confirms the importance of the warning given by [Morisset \(2017\)](#) who, through photoionization models, predict large errors in the determination of the physical conditions and chemical abundances in nebulae when one assumes a single component when in reality there are several. The exercise we present in this section is an observational confirmation.

If instead of using the classical diagnostics to determine  $n_e$ , we consider the average of the densities of each component (See Table 3), weighed by their observed  $f(\text{H}\beta)$ , we get:  $n_e = 6820 \pm 810$ . This value is roughly between the predictions of classical diagnostics and  $n_e([\text{Fe III}])$ . Note that in Fig. 17, close to this value

**Figure 18.** Normalized  $f([\text{O II}] \lambda 3727)$  in the spectrum that results from adding all the spatial pixels in the UVES slit. Each of the velocity components are identified.

of density,  $T_e([\text{O II}])$  and  $T_e([\text{S II}])$  converge to  $T_e([\text{N II}])$ . Using that density, we obtain:  $T_e([\text{O II}]) = 8650^{+410}_{-520}$ ,  $T_e([\text{S II}]) = 9890^{+1100}_{-990}$ ,  $T_e([\text{N II}]) = 8850^{+210}_{-180}$ ,  $T_e([\text{S III}]) = 8800^{+250}_{-160}$  and  $T_e([\text{O III}]) = 8490^{+90}_{-120}$ . Calculating the ionic abundances of oxygen with these physical conditions, we obtain:  $\text{O}^+ = 8.36^{+0.06}_{-0.05}$  and  $\text{O}^{2+} = 7.64 \pm 0.02$ , which implies  $\text{O} = 8.44 \pm 0.05$ . Values more consistent with those of the individual components.

The effects of what has been discussed in this section can be



clearly observed in Fig. 2 from O'Dell et al. (2017a). That figure shows the spatial distribution of  $n_e$  ([S II]) and  $T_e$  ([N II]) derived in a pseudo-slit created with MUSE 2D spectroscopic data (Weilbacher et al. 2015), covering a zone close to our observations, but with lower spectral resolution and integrating the emission of HH 204, the Blue Layer and the nebular gas. It can be seen that as one approaches the bowshock from the direction of the jet,  $n_e$  ([S II]) increases, reaching a zone where its value stabilizes around  $\sim 5000 \text{ cm}^{-3}$  and decreasing again as one moves outwards the bowshock. On the other hand,  $T_e$  ([N II]) initially fluctuates at around  $\sim 8500 \text{ K}$  but once we are in the area where  $n_e$  ([S II]) is high and constant,  $T_e$  ([N II]) begins to increase, until reaching a maximum value of  $\sim 9500 \text{ K}$ . Once the density drops,  $T_e$  ([N II]) again reaches values that fluctuate around  $\sim 8500 \text{ K}$ . A similar behavior was observed by Mesa-Delgado et al. (2008) and Núñez-Díaz et al. (2012) at the edge of the bowshock of HH 204. Those authors associate the peak in  $T_e$  ([N II]) with shock heating of the gas.

What actually happens in Fig. 2 of O'Dell et al. (2017a) is that  $n_e$  ([S II]) – the density diagnostic they use – is not able to effectively account for the increase in density due to the compression of the gas in HH 204. As shown in Fig. 5, when approaching the bowshock, the density of HH 204 steadily increases up to  $\sim 20000 \text{ cm}^{-3}$  at the bowshock, not a zone of stabilization of density when one approaches the bowshock (located around the value 3.2 on the x-axis of Fig. 2 from O'Dell et al. 2017a). As  $T_e$  ([N II]) diagnostic tends to be density sensitive for values larger than  $\sim 1000 \text{ cm}^{-3}$ , an underestimation of  $n_e$  imply an overestimation of  $T_e$  and consequently, a significant underestimation of ionic abundances based on CELs, which are highly dependent on temperature.

In the case of our observations, the different density components have different radial velocities, which can be successfully separated thanks to our high spectral resolution. However, one might wonder how many internal jets or gas lumps having velocities similar to that of the bulk of the ionized gas can exist in the Orion Nebula. These unresolved components, being integrated along the line of sight, may affect the determination of the true physical and chemical properties of the nebula.

## 8 DISCUSSION

In this second paper of our series dedicated to photoionized HHe objects in the Orion Nebula, we study HH 204. Our spectroscopical observations correspond to the slit shown in Fig. 1. The high spectral resolution ( $\lambda/\Delta\lambda \approx 6.5 \text{ km s}^{-1}$ ) allows to identify and properly separate 3 components of ionized gas: the diffuse Blue Layer, the emission of the Orion Nebula and HH 204. In the following we will discuss the results concerning each of these components.

### 8.1 The Diffuse Blue Layer

The component designated as Blue Layer was firstly reported by Deharveng (1973), although it has been little studied, since a very high spectral resolution is required to be able to separate its emission from that of the Orion Nebula. García-Díaz & Henney (2007) analyzed the velocity structure of the Orion Nebula through the emission of [O II], [S II] and [S III] lines, using echelle spectroscopy. They detected the emission of the [S II] doublet from the Diffuse Blue Layer, estimating a density of  $\sim 400 \text{ cm}^{-3}$ , which is in complete agreement with our estimates. These authors did not detect the emission of [O I] or [S III] in this component, although the emission of other low ionization ions such as [O II] and [N II] was detected

in previous works (Jones 1992; Henney & O'Dell 1999). These limited spectroscopical evidences lead to interpret the Diffuse Blue Layer as composed by fully ionized gas, whose ionizing radiation field was rather soft, probably coming from  $\theta^2$  Ori A. However, we do detect [O I] and [S III] lines in the spectrum of this component extracted from cut 2 (figs. 19 and 20). In fact, we also detect a weak emission of [O III], indicative of the presence of gas with a high degree of ionization.

Through observations of HI 21-cm emission, van der Werf et al. (2013) determined the existence of several HI velocity components in the Orion Nebula. At the southeast, in the area where the Diffuse Blue Layer is located, these authors identified a blueshifted component named ‘D’ and interpreted it as an expanding shell centered on  $\theta^2$  Ori B, which is consistent with a scenario where this star ionizes the gas of the Diffuse Blue Layer. The observed [O I] emission is consistent with the presence of an ionization front (IF) in this nebular feature. However, with the new information provided by the ionic abundances of the Diffuse Blue Layer – estimated for the first time in this work – the simple model where the gas is photoionized exclusively by  $\theta^2$  Ori B may not be correct. Although small, the contribution of  $\text{O}^{2+}$  to the total abundance is not negligible, being around 10%. On the other hand, assuming that the Diffuse Blue Layer should have a chemical composition similar to the Orion Nebula, this implies that the estimated  $\text{N}^+$  abundance is approximately 75% of the total nitrogen abundance, therefore the contribution of  $\text{N}^{2+}$  should be significant. Since  $\theta^2$  Ori B is a B0.7V star (Simón-Díaz 2010), we do not expect such a star to emit a significant number of photons capable of maintaining a considerable proportion of highly ionized ions. This is reinforced by the spectroscopical results of Galactic H II regions ionized by B-type stars such as Sh 2-32, Sh 2-47, Sh 2-82, Sh 2-175, Sh 2-219, Sh 2-270, Sh 2-285, Sh 2-297 and IC 5146 (García-Rojas et al. 2014; Esteban & García-Rojas 2018; Arellano-Córdova et al. 2020a). In all these regions, the nitrogen is only once ionized and the contribution of  $\text{O}^{2+}$  to the total oxygen is lower than 2%, with the exception of the faint Sh 2-47, although in this case, the  $\text{O}^{2+}$  abundance determination is very uncertain.

As we can see in the discussion above, the spectroscopical properties of the Diffuse Blue Layer suggest some ionization by radiation leakage from the Orion Nebula. Simón-Díaz et al. (2011) found abnormal emission of CELs of high-ionized species (mainly [O III]) in the external zones of M 43, an H II region located at the northeast of the Orion Nebula which is ionized by a B0.5V star. As those authors demonstrate, the spectral properties of this abnormal emission is consistent with contamination by scattered light from the Huygens Region. In our case, we can discard the scattered nature of the emission of high-ionized ions in the Diffuse Blue Layer because (i) it has the same velocity as the low-ionization ion lines, (ii) we do not detect anomalies in the Balmer decrement of the spectrum of the Diffuse Blue Layer, that would be a signature of the presence of scattered emission (see Simón-Díaz et al. 2011). New observations with longer exposure time, similar spectral resolution and covering different areas of the Orion Nebula would shed more light on the physical, chemical and geometrical properties of the Diffuse Blue Layer.

### 8.2 The Nebular Component

There are notable differences in the degree of ionization and physical conditions of the gas of the nebular component studied in this work and in Paper I. The degree of ionization in the area of the Orion Nebula observed in this paper is  $\text{O}^{2+}/\text{O} = 0.42 \pm 0.04$  while in

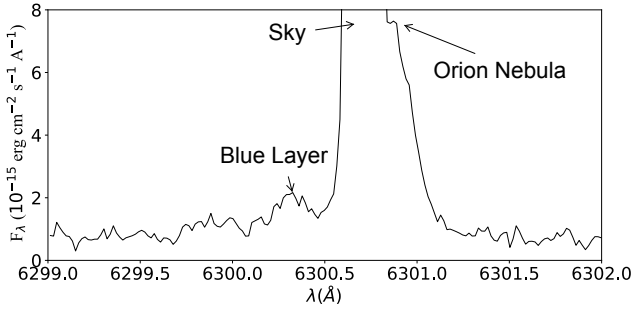


**Figure 19.** Spectrum of cut 2 showing the emission of [O I]  $\lambda 6300$  of the Diffuse Blue Layer and the Orion Nebula.

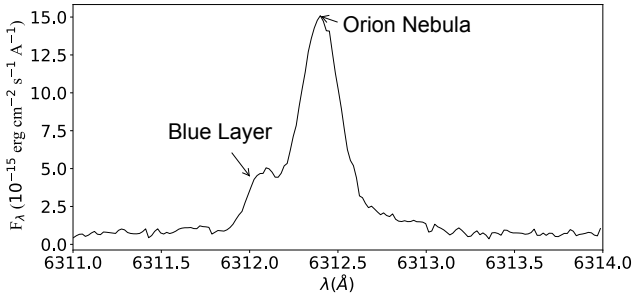


**Figure 20.** Spectrum of cut 2 showing the emission of [S III]  $\lambda 6312$  of the Diffuse Blue Layer and the Orion Nebula.

that observed in Paper I is  $\sim 0.8$ . This is an expected behavior considering the different distances of both areas with respect to the main ionizing source. The density in the nebular component in the direction of HH 204 is  $n_e = 1440 \pm 170 \text{ cm}^{-3}$ , significantly lower than the values of  $n_e \sim 6000 \text{ cm}^{-3}$  estimated around HH 529II and III in Paper I. This result, is again consistent with the more external position of HH 204 with respect to  $\theta^1$  Ori C and to the centre of a blister-shaped nebula. There is a remarkable consistency between the  $T_e(\text{[O III]})$  and  $T_e(\text{[N II]})$  values we obtain with the predictions of the radial distribution of those quantities given in eqs. 4 and 5 of Mesa-Delgado et al. (2008), confirming that the temperature decreases linearly with the radial distance from  $\theta^1$  Ori C.

As expected, the total abundances of O, N, S and Cl shown in Table 6 are in good agreement with those shown in Table 11 of Paper I. However, the abundances of Ne and Ar are somewhat different because the use of different ICFs to estimate the contribution of unseen  $\text{Ar}^+$  and  $\text{Ne}^+$ , which in this work have a greater impact, due to the lower degree of ionization of the nebular component in the direction to HH 204. A similar situation occurs with the C abundance, which requires large corrections to estimate the important contribution of  $\text{C}^+$ . Although the total abundance of  $\text{O} = 8.42 \pm 0.04$  we obtain using CELs is entirely consistent with the value of  $\text{O} = 8.46 \pm 0.03$  derived in Paper I, both are somewhat

lower than the value of  $\text{O} = 8.51 \pm 0.03$  obtained by Esteban et al. (2004) and Mesa-Delgado et al. (2009) in two different areas of the Orion Nebula. It is interesting to note that this difference seems to be correlated with the abundance discrepancy factor (ADF) of  $\text{O}^{2+}$  estimated in each observed area. The values of  $\text{ADF}(\text{O}^{2+})$  are 0.36, 0.20, 0.13 and 0.11 for the nebular component of this work, Paper I, Esteban et al. (2004) and Mesa-Delgado et al. (2009), respectively. If we recalculate the abundance of  $\text{O}^{2+}$  based on CELs reducing the  $\text{ADF}(\text{O}^{2+})$  to 0.12, we would obtain  $\text{O} = 8.53 \pm 0.03$  for both, the value obtained in this work and in Paper I, matching the values obtained by Esteban et al. (2004) and Mesa-Delgado et al. (2009) within the uncertainties. If in all cases, we recalculate the  $\text{O}^{2+}$  abundance assuming  $\text{ADF} = 0$ , the four aforementioned determinations of the total oxygen abundance in the component of the Orion Nebula converge to  $\sim 8.6$ . In any case, there are other explanations for the different O abundances obtained in different zones of the nebula. One can be related to a different depletion factor of O onto dust grains across the Orion Nebula. This element may be trapped in the form of oxides, pyroxenes or olivines, compounds that would include atoms of metals such as Fe. The total abundance of Fe does not differ substantially between the aforementioned four zones of the Orion Nebula, and the relatively large uncertainties associated with the Fe do not permit to trace differences in the depletion factor of O.

### 8.3 HH 204

Our spectroscopic observations allow the analysis of the physical conditions and ionic abundances of HH 204 in unprecedented detail. The results show that the gas is compressed as it approaches the bowshock, increasing its density. On the other hand,  $T_e(\text{[N II]})$  and  $T_e(\text{[S III]})$  remain unaltered by the shock, being consistent with the expected values for a gas in photoionization equilibrium, while  $T_e(\text{[O III]})$  seems to be altered, reaching the maximum values at the bowshock and decreasing when moving away – towards the interior of the jet – from this point until its value stabilizes to temperatures more similar to those given by the rest of diagnostics. This behavior of  $T_e(\text{[O III]})$  may be related to collisional ionization of a small number of  $\text{O}^+$  ions. Due to the increase in density when approaching the bowshock and the distance to  $\theta^1$  Ori C, the degree of ionization, measured as the  $\text{O}^{2+}/\text{O}$  ratio, drops almost to zero. In fact, the density increase is enough to trap an ionization front, that becomes evident through the detection of emission lines of neutral elements such as [O I] and [N I]. This aspect deserves further discussion. In previous studies, the detection of lines of neutral species has been interpreted as product of the interaction of HH 204 with neutral material, such as that found in the Orion's Veil (O'Dell et al. 1997a,b; Takami et al. 2002). However, there are several arguments against this scenario and in favor of the trapped ionization front. (i) The spatial distribution of the [O I] emission, shown in Fig. 2, is more concentrated than that of [O II] or [O III], located at the southeast of HH 204, in the opposite direction to  $\theta^1$  Ori C, consistent with a zone shielded from the ionizing radiation. (ii) The combination of the tangential and radial motions of HH 204 allows to know its 3D-trajectory. From its apparent distance to Orion-S (its likely origin), Doi et al. (2004) estimate that HH 204 has moved  $\sim 0.15 \text{ pc}$  radially towards the observer. Although van der Werf et al. (2013) argued that the Orion Veil lays  $\sim 0.3 \text{ pc}$  apart from Orion-S, Abel et al. (2016) established that the distance must be significantly larger and therefore a direct interaction with the Veil is unlikely. If those distance estimations are correct, HH 204 would be located within the main ionized gas of the Orion Nebula or

interacting with the Nearer Ionized Layer (NIL) (Abel et al. 2019; O'Dell et al. 2020). (iii) The  $T_e(\text{[O II]})$  we obtain for HH 204 is incompatible with entrained material from a neutral region such as the Veil, which would have a temperature of a few hundred K. (Abel et al. 2006).

In HH 204, the  $\text{O}^+$  abundances calculated with RLs and with CELs coincide. Since in this object practically all the oxygen is once ionized only, this implies that HH 204 – contrary to what is usually found in ionized nebulae – does not show an ADF in both,  $\text{O}^+$  and O abundances. In Sec. 5.2 we discussed 3 phenomena that may be the cause of the ADF and that in HH 204 have a negligible impact: (i) temperature fluctuations, (ii) starlight fluorescence and (iii) chemical or density inhomogeneities. The consistency of the O abundances determined from RLs and CELs in HH 204 suggests that its true value should be  $\sim 8.6$ , lower than the recommended solar O abundance ( $8.73 \pm 0.07$ , Lodders 2019).

In Table 7 we compile the O abundances obtained in all chemical abundance studies of the Orion Nebula based on deep echelle spectroscopy taken with UVES. A note of caution should be given because any comparison among the abundances of the different zones must consider that a fraction of O may be depleted onto dust grains. For example, Mesa-Delgado et al. (2009) estimated such fraction to be  $\sim 0.12$  dex. However, the amount of O in dust grains may change across the nebula and be lowered by destruction of dust grains due to the passage of shocks, specially in the HH objects. We recommend to consider an extra uncertainty of  $\sim 0.05$  dex to any given O abundance to include unaccounted depletion variations.

If we assume that the O abundances based on RLs are the true ones in all objects, we have some issues to consider. Firstly, For example, HH 529 II and III and other zones of the Orion Nebula show larger O/H ratios than the rest. In Paper I we discuss the possibility of having a slight overmetallicity in HH 529 II and III, due to the entrainment of material from the accretion disk of the stellar source of the jets. On the other hand, the O abundances based on RLs found in the nebular components studied in Paper I and Esteban et al. (2004) are also somewhat higher than what is found in HH 204. These differences may have different explanations in each case, apart from the previously mentioned dust depletion variations.

Conversely, if we assume that the O abundances based on CELs are the true ones, we could reconcile all the observed values simply by considering different proportions of O depletion onto dust grains in addition to small contributions from other phenomena as, for example, temperature inhomogeneities. In this context, if we assume that half of the difference between  $\sim 8.6$  – considering that the O abundance obtained from both, CELs and RLs in HH 204 is the true one of the Orion Nebula – and the O abundance based on CELs obtained by Esteban et al. (2004) is due to dust depletion and the rest to temperature fluctuations, this would be compatible with  $t^2 \sim 0.008$ , a value considerable smaller than the  $t^2 \sim 0.022$  necessary to match the O abundances based on RLs from the same spectrum. In this case, the important question is why the RLs are giving higher O abundances in all cases except HH 204. An important difference between the determination of O abundance in HH 204 and the other zones or objects is that, in HH 204, the contribution of  $\text{O}^{2+}$  to the total abundance is negligible. It is important to say that Mesa-Delgado et al. (2009) also obtain an ADF( $\text{O}^+$ ) equal to zero in both, the nebular component and HH 202 S. However, the contribution of  $\text{O}^{++}$  is important in those spectra and their ADF( $\text{O}^{2+}$ ) are not zero. This result can give clues about the possible origin of the AD problem. We will further explore this interesting point in future papers of this series.

The low ionization degree of HH 204 is an advantage for determining the abundance of certain elements. In areas close to the bowshock, where the ionization degree drops to practically zero, we can obtain the total abundance of N, S, Cl, Fe and Ni without the use of an ICF, simply adding the ionic abundances determined from our optical spectrum. This makes it possible to eliminate the generally most important source of uncertainty and thus obtain very precise determinations of the given abundances, which can be used as representative of the Orion Nebula. The opposite side of this advantage is that the elements that only show optical lines of high ionization potential ions, as He or Ne, need very large ICFs in the conditions of HH 204, and their total abundances cannot be derived with good precision.

From Table 6, it is clear that the Fe abundance in HH 204 is higher than in the other components due to dust destruction in the bowshock. Following the same procedure as in Paper I, comparing the observed Fe/O values in HH 204 and the nebular component with the expected solar value (Lodders 2019), we estimate that  $\sim 6\%$  of the total Fe is in the gaseous phase in the nebular component, while this fraction goes up to 21% in HH 204, representing an increase of a factor 3.5. In HH 204 we have probably estimated the most accurate total abundance of Ni in the literature. In Sec. 4.3, we determined that the once and twice ionized ions of Fe and Ni coexist basically in the same nebular volumes and exhibit similar depletion patterns. We obtain  $\log(\text{Fe}^+/\text{Ni}^+) = 1.26 \pm 0.03$ ,  $\log(\text{Fe}^{2+}/\text{Ni}^{2+}) = 1.37 \pm 0.03$  and  $\log(\text{Fe}/\text{Ni}) = 1.33 \pm 0.03$ , values consistent with the solar ratio (Lodders 2019). However, the  $\text{Ni}^{2+}$  abundance may be slightly lower due to some inaccuracies found in the atomic data.

#### 8.4 On the presence of high-density inclusions

Last but not least we want to discuss the influence of the presence of a high-density component in the spectrum of a photoionized region when it is not detected in the observations. We have studied this scenario in Sec. 7 adding the nebular emission from the Orion Nebula, the Diffuse Blue Layer and HH 204, which would be obtained when observing with a velocity resolution lower than  $\sim 54 \text{ km s}^{-1}$  or  $R \approx 5550$ . In this case, the classical density diagnostics such as  $I(\text{[O II] } \lambda 3726)/I(\text{[O II] } \lambda 3729)$ ,  $I(\text{[S II] } \lambda 6716)/I(\text{[S II] } \lambda 6731)$  and  $I(\text{[Cl III] } \lambda 5518)/I(\text{[Cl III] } \lambda 5538)$  are not sensitive to the high density of HH 204, which is beyond the critical densities of the levels that give rise to the lines of the diagnostics. In the case of the first two mentioned diagnostics, the resulting density is biased towards the values of the Orion Nebula and the Diffuse Blue Layer. Although the [Cl III] is sensitive at somewhat higher densities, it traces specially the conditions of the Orion Nebula because its higher ionization degree. The incorrectly lower density values determined with those diagnostics produce an overestimation of  $T_e(\text{[N II]})$ . Since the contribution of low ionization degree ions is important in all components, this implies an important underestimation of the abundances of some elements. In the case of  $\text{O}^+$ , the underestimation would be  $\sim 0.2$  dex (see Sec. 7), producing a similar impact on the total O abundance, as  $\text{O}^+$  is the dominant ion. However, the problem affects indirectly to other elements which total abundance is based on highly ionized ions through the ICFs. This is because they depend on the degree of ionization, measured as  $\text{O}^{2+}/(\text{O}^{2+} + \text{O}^+)$ . The impact of high-density inclusions or components onto the abundances will depend on the integrated volume, degree of ionization and density.

Previous studies of the area based on lower spectral resolution spectroscopy reported localized increases of  $T_e(\text{[N II]})$  (Mesa-Delgado et al. 2008; Núñez-Díaz et al. 2012; O'Dell et al. 2017a), which were interpreted as the product of shock heating. The re-

**Table 7.** Oxygen abundances in the Orion Nebula based on UVES spectroscopy.

Region	O <sup>+</sup>	RLs O <sup>2+</sup>	O	O <sup>+</sup>	CELs O <sup>2+</sup>	O	Reference
Orion Nebula	8.15 ± 0.13	8.57 ± 0.01	8.71 ± 0.03	7.76 ± 0.15	8.43 ± 0.01	8.51 ± 0.03	Esteban et al. (2004)
	8.01 ± 0.12	8.46 ± 0.03	8.59 ± 0.05	8.00 ± 0.06	8.35 ± 0.03	8.51 ± 0.03	Mesa-Delgado et al. (2009)
	8.25 ± 0.06	8.52 ± 0.02	8.70 ± 0.03	7.83 ± 0.05	8.35 ± 0.03	8.46 ± 0.03	Mendez Delgado & Amigos (2021)
	-	8.40 ± 0.03	8.60 ± 0.03*	8.18 ± 0.06	8.04 ± 0.02	8.42 ± 0.04	This work
HH 202 S	8.25 ± 0.16	8.44 ± 0.03	8.65 ± 0.05	8.29 ± 0.06	8.08 ± 0.03	8.50 ± 0.04	Mesa-Delgado et al. (2009)
HH 529 II	<7.91	8.83 ± 0.07	8.83 ± 0.07	7.36 ± 0.12	8.54 ± 0.03	8.57 ± 0.03	Mendez Delgado & Amigos (2021)
HH 529 III	<7.95	8.84 ± 0.09	8.84 ± 0.09	7.51 ± 0.22	8.48 ± 0.03	8.53 ± 0.03	Mendez Delgado & Amigos (2021)
HH 204	8.57 ± 0.03	<7.54	<b>8.57 ± 0.03</b>	8.62 ± 0.05	6.34 ± 0.02	<b>8.62 ± 0.05</b>	This Work

\* The abundance of O<sup>+</sup> based on CELs was used.

sults presented in Sec. 5 demonstrate that this interpretation is not correct. This apparent peak of  $T_e$  ([N II]) is produced artificially because the use of  $n_e$  values that are not the true ones. In the case of  $T_e$  ([O III]) the effects observed in HH 204, which are due to the shock, go unnoticed since HH 204 presents a very low ionization degree. In Table 3 we can see that, for HH 204, even the classical density diagnostics give values consistent with those obtained from the ratio of [Fe III] lines. This is because HH 204, due to its orientation and the spectral resolution of the observations, can be interpreted basically as a single high-density slab of gas. This would be different in the case of an HH object observed with low resolution spectroscopy moving directly towards the observer. We would most likely have a density gradient in the line of sight, because it will cross the compressed gas at the bowshock and the less denser material traveling behind along the jet. In this or similar situations, a way to detect the presence of high-density inclusions can be the use of the  $I([\text{Fe III}] \lambda 4658)/I([\text{Fe III}] \lambda 4702)$  ratio as a density diagnostic. This ratio is practically density insensitive at values smaller than  $\sim 10^3 \text{ cm}^{-3}$ , while its critical density is above  $\sim 10^6 \text{ cm}^{-3}$ . In the case of a gas inclusion with density of around or larger than  $\sim 10^4 \text{ cm}^{-3}$  in a region with an overall density of  $10^2 - 10^3 \text{ cm}^{-3}$ , this diagnostic will be biased to the higher density component, while classical ones will be biased in the opposite direction. A significant discrepancy between the [Fe III] diagnostic and classical ones in a region of apparently low  $n_e$  may serve as an indicator of this type of situations.

## 9 CONCLUSIONS

### ACKNOWLEDGEMENTS

This work is based on observations collected at the European Southern Observatory, Chile, proposal number ESO 092.C-0323(A) **C: Esta frase tiene que incluirse en el artículo de HH529.** We acknowledge support from the Agencia Estatal de Investigación del Ministerio de Ciencia e Innovación (AEI-MCINN) under grant *Espectroscopía de campo integral de regiones H II locales. Modelos para el estudio de regiones H II extragalácticas* with reference 10.13039/501100011033. JG-R acknowledges support from an Advanced Fellowship from the Severo Ochoa excellence program (SEV-2015-0548). JEM-D thanks the support of the Instituto de Astrofísica de Canarias under the Astrophysicist Resident Program and acknowledges support from the Mexican CONACyT (grant CVU 602402). The authors acknowledge support under grant P/308614 financed by funds transferred from the Spanish Ministry of Science, Innovation and Universities, charged to the General State

Budgets and with funds transferred from the General Budgets of the Autonomous Community of the Canary Islands by the MCIU.

## REFERENCES

- Abel N. P., Ferland G. J., O'Dell C. R., Shaw G., Troland T. H., 2006, *ApJ*, **644**, 344
- Abel N. P., Ferland G. J., O'Dell C. R., Troland T. H., 2016, *ApJ*, **819**, 136
- Abel N. P., Ferland G. J., O'Dell C. R., 2019, *ApJ*, **881**, 130
- Arellano-Córdova K. Z., Esteban C., García-Rojas J., Méndez-Delgado J. E., 2020a, arXiv e-prints, [p. arXiv:2012.06643](https://arxiv.org/abs/2012.06643)
- Arellano-Córdova K. Z., Esteban C., García-Rojas J., Méndez-Delgado J. E., 2020b, *MNRAS*, **496**, 1051
- Baldwin J. A., et al., 1996, *ApJ*, **468**, L115
- Bally J., Sutherland R. S., Devine D., Johnstone D., 1998, *AJ*, **116**, 293
- Bautista M. A., 2001, *A&A*, **365**, 268
- Bautista M. A., 2004, *A&A*, **420**, 763
- Bautista M. A., Pradhan A. K., 1998, *ApJ*, **492**, 650
- Bautista M. A., Peng J., Pradhan A. K., 1996, *ApJ*, **460**, 372
- Bautista M. A., Fivet V., Ballance C., Quinet P., Ferland G., Mendoza C., Kallman T. R., 2015, *ApJ*, **808**, 174
- Bhatia A. K., Kastner S. O., 1995, *ApJS*, **96**, 325
- Binder B. A., Povich M. S., 2018, *ApJ*, **864**, 136
- Blagrove K. P. M., Martin P. G., Baldwin J. A., 2006, *ApJ*, **644**, 1006
- Blagrove K. P. M., Martin P. G., Rubin R. H., Dufour R. J., Baldwin J. A., Hester J. J., Walter D. K., 2007, *ApJ*, **655**, 299
- Butler K., Zeppen C. J., 1989, *A&A*, **208**, 337
- Canto J., Goudis C., Johnson P. G., Meaburn J., 1980, *A&A*, **85**, 128
- D'Odorico S., Cristiani S., Dekker H., Hill V., Kaufer A., Kim T., Primas F., 2000, Performance of UVES, the echelle spectrograph for the ESO VLT and highlights of the first observations of stars and quasars. pp 121–130, [doi:10.1117/12.390133](https://doi.org/10.1117/12.390133)
- Davey A. R., Storey P. J., Kisielius R., 2000, *A&AS*, **142**, 85
- Deharveng L., 1973, *A&A*, **29**, 341
- Doi T., O'Dell C. R., Hartigan P., 2004, *AJ*, **127**, 3456
- Esteban C., García-Rojas J., 2018, *MNRAS*, **478**, 2315
- Esteban C., Peimbert M., Torres-Peimbert S., Escalante V., 1998, *MNRAS*, **295**, 401
- Esteban C., Peimbert M., García-Rojas J., Ruiz M. T., Peimbert A., Rodríguez M., 2004, *MNRAS*, **355**, 229
- Esteban C., García-Rojas J., Pérez-Mesa V., 2015, *MNRAS*, **452**, 1553
- Fritzche S., Fricke B., Geschke D., Heitmann A., Sienkiewicz J. E., 1999, *ApJ*, **518**, 994
- Froese Fischer C., Tachiev G., 2004, *Atomic Data and Nuclear Data Tables*, **87**, 1
- Froese Fischer C., Rubin R. H., Rodríguez M., 2008, *MNRAS*, **391**, 1828
- Gaia Collaboration et al., 2018, *A&A*, **616**, A1
- Galavis M. E., Mendoza C., Zeppen C. J., 1995, *A&AS*, **111**, 347
- García-Díaz M. T., Henney W. J., 2007, *AJ*, **133**, 952



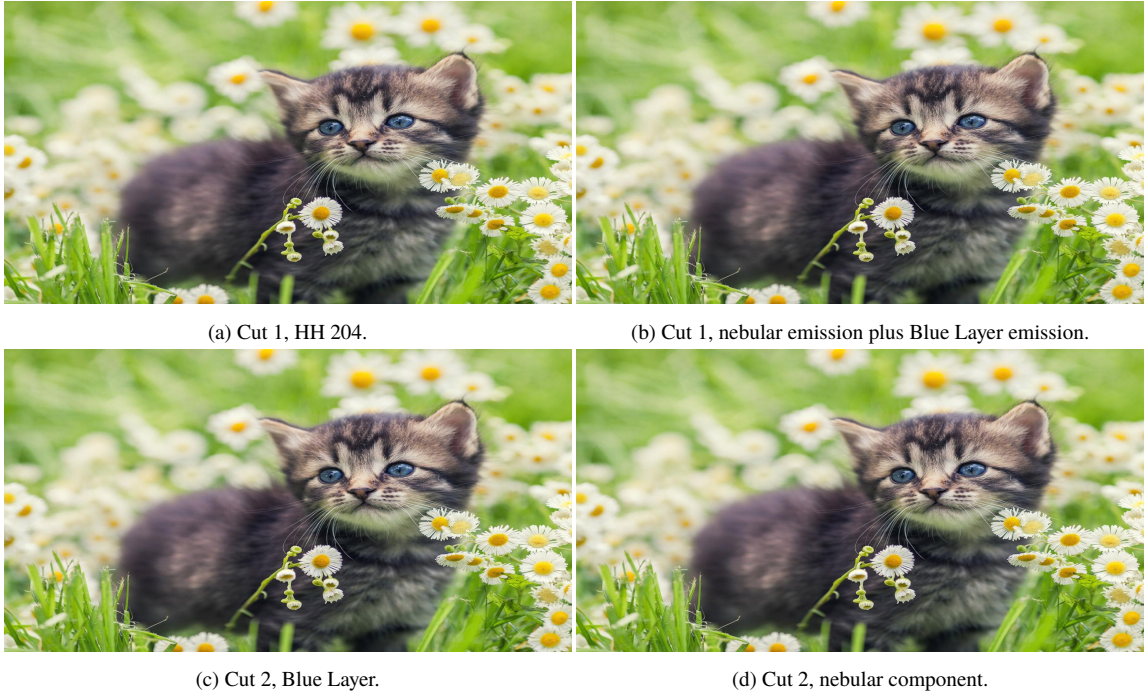
- García-Díaz M. T., Henney W. J., López J. A., Doi T., 2008, *Rev. Mex. Astron. Astrofis.*, **44**, 181
- García-Rojas J., Simón-Díaz S., Esteban C., 2014, *A&A*, **571**, A93
- Grieve M. F. R., Ramsbottom C. A., Hudson C. E., Keenan F. P., 2014, *ApJ*, **780**, 110
- Henney W. J., O'Dell C. R., 1999, *AJ*, **118**, 2350
- Henney W. J., O'Dell C. R., Zapata L. A., García-Díaz M. T., Rodríguez L. F., Robberto M., 2007, *AJ*, **133**, 2192
- Johansson S., Zethson T., Hartman H., Ekberg J. O., Ishibashi K., Davidson K., Gull T., 2000, *A&A*, **361**, 977
- Jones M. R., 1992, PhD thesis, RICE UNIVERSITY.
- Kaufman V., Sugar J., 1986, *Journal of Physical and Chemical Reference Data*, **15**, 321
- Kisieliński R., Storey P. J., Ferland G. J., Keenan F. P., 2009, *MNRAS*, **397**, 903
- Lodders K., 2019, arXiv e-prints, [p. arXiv:1912.00844](https://arxiv.org/abs/1912.00844)
- Lucy L. B., 1995, *A&A*, **294**, 555
- Luridiana V., Morisset C., Shaw R. A., 2015, *A&A*, **573**, A42
- McLaughlin B. M., Lee T.-G., Ludlow J. A., Landi E., Loch S. D., Pindzola M. S., Ballance C. P., 2011, *Journal of Physics B Atomic Molecular Physics*, **44**, 175206
- Meléndez M., Bautista M. A., Badnell N. R., 2007, *A&A*, **469**, 1203
- Mendez Delgado J. E., Amigos G., 2021
- Mendoza C., 1983, in Aller L. H., ed., *IAU Symposium Vol. 103, Planetary Nebulae*. pp 143–172
- Mendoza C., Zeppen C. J., 1982, *MNRAS*, **198**, 127
- Mendoza C., Zeppen C. J., 1983, *MNRAS*, **202**, 981
- Mesa-Delgado A., Esteban C., García-Rojas J., 2008, *ApJ*, **675**, 389
- Mesa-Delgado A., Esteban C., García-Rojas J., Luridiana V., Bautista M., Rodríguez M., López-Martín L., Peimbert M., 2009, *MNRAS*, **395**, 855
- Moehler S., Dreizler S., LeBlanc F., Khalack V., Michaud G., Richer J., Sweigart A. V., Grundahl F., 2014a, *A&A*, **565**, A100
- Moehler S., et al., 2014b, *A&A*, **568**, A9
- Morisset C., 2017, in Liu X., Stanghellini L., Karakas A., eds, Vol. 323, *Planetary Nebulae: Multi-Wavelength Probes of Stellar and Galactic Evolution*. pp 43–50 ([arXiv:1612.04242](https://arxiv.org/abs/1612.04242)), [doi:10.1017/S1743921317001004](https://doi.org/10.1017/S1743921317001004)
- Münch G., Wilson O. C., 1962, *Z. Astrophys.*, **56**, 127
- Núñez-Díaz M., Mesa-Delgado A., Esteban C., López-Martín L., García-Rojas J., Luridiana V., 2012, *MNRAS*, **421**, 3399
- Nussbaumer H., Storey P. J., 1982, *A&A*, **110**, 295
- O'Dell C. R., Hartigan P., Lane W. M., Wong S. K., Burton M. G., Raymond J., Axon D. J., 1997a, *AJ*, **114**, 730
- O'Dell C. R., Hartigan P., Bally J., Morse J. A., 1997b, *AJ*, **114**, 2016
- O'Dell C. R., Peimbert M., Peimbert A., 2003, *AJ*, **125**, 2590
- O'Dell C. R., Ferland G. J., Henney W. J., Peimbert M., García-Díaz M. T., Rubin R. H., 2015, *AJ*, **150**, 108
- O'Dell C. R., Ferland G. J., Peimbert M., 2017a, *MNRAS*, **464**, 4835
- O'Dell C. R., Kollatschny W., Ferland G. J., 2017b, *ApJ*, **837**, 151
- O'Dell C. R., Abel N. P., Ferland G. J., 2020, *ApJ*, **891**, 46
- Osterbrock D. E., Tran H. D., Veilleux S., 1992, *ApJ*, **389**, 305
- Peimbert M., 1967, *ApJ*, **150**, 825
- Pequignot D., Petitjean P., Boisson C., 1991, *A&A*, **251**, 680
- Podobedova L. I., Kelleher D. E., Wiese W. L., 2009, *Journal of Physical and Chemical Reference Data*, **38**, 171
- Porter R. L., Ferland G. J., Storey P. J., Detisch M. J., 2012, *MNRAS*, **425**, L28
- Porter R. L., Ferland G. J., Storey P. J., Detisch M. J., 2013, *MNRAS*, **433**, L89
- Quinet P., 1996, *A&AS*, **116**, 573
- Quinet P., Le Dourneuf M., 1996, *A&AS*, **119**, 99
- Ramsbottom C. A., Bell K. L., 1997, *Atomic Data and Nuclear Data Tables*, **66**, 65
- Rodríguez M., 1999, *A&A*, **348**, 222
- Rodríguez M., Rubin R. H., 2005, *ApJ*, **626**, 900
- Simón-Díaz S., 2010, *A&A*, **510**, A22
- Simón-Díaz S., García-Rojas J., Esteban C., Stasińska G., López-Sánchez A. R., Morisset C., 2011, *A&A*, **530**, A57
- Stasińska G., 1978, *A&A*, **66**, 257
- Storey P. J., Hummer D. G., 1995, *MNRAS*, **272**, 41
- Storey P. J., Zeppen C. J., 2000, *MNRAS*, **312**, 813
- Storey P. J., Sochi T., Badnell N. R., 2014, *MNRAS*, **441**, 3028
- Storey P. J., Sochi T., Bastin R., 2017, *MNRAS*, **470**, 379
- Takami M., et al., 2002, *ApJ*, **566**, 910
- Tayal S. S., 2004, *A&A*, **418**, 363
- Tayal S. S., 2011, *ApJS*, **195**, 12
- Tayal S. S., Zatsarinny O., 2010, *ApJS*, **188**, 32
- Tayal S. S., Zatsarinny O., 2020, *ApJ*, **888**, 10
- Verner E. M., Verner D. A., Baldwin J. A., Ferland G. J., Martin P. G., 2000, *ApJ*, **543**, 831
- Weilbacher P. M., et al., 2015, *A&A*, **582**, A114
- Wiese W. L., Fuhr J. R., Deters T. M., 1996, *Journal of Physical and Chemical Reference Data*, Monograph 7, 403
- Zel'dovich Y. B., Raizer Y. P., 1967, *Physics of shock waves and high-temperature hydrodynamic phenomena*
- Zhang H. L., Pradhan A. K., 1997, *A&AS*, **126**, 373
- Zhang, Hong Lin 1996, *Astron. Astrophys. Suppl. Ser.*, **119**, 523
- van der Werf P. P., Goss W. M., O'Dell C. R., 2013, *ApJ*, **762**, 101

**APPENDIX A: SOME EXTRA MATERIAL**

This paper has been typeset from a  $\text{\LaTeX}$  file prepared by the author.

**Table A1.** Spatial distribution of physical conditions and ionic abundances along HH 204 as a function of the distance from the bowshock. Values derived from the blue arm spectrum.

Distance (mpc)	$n_e([Fe\ III])$ ( $cm^{-3}$ )	$T_e([O\ III])$ (K)	He <sup>+</sup> ( $\lambda 4471$ )	O <sup>+</sup> log. units with $n(H)=12$	O <sup>2+</sup>	Ne <sup>2+</sup>
0.00	19610 ± 4590	16820 ± 760	10.50 ± 0.02	8.66 ± 0.11	7.01 ± 0.06	-
0.49	18870 ± 4420	17200 ± 650	10.46 ± 0.01	8.67 ± 0.12	6.87 ± 0.06	-
0.98	19640 ± 4450	18570 ± 600	10.46 ± 0.01	8.70 ± 0.09	6.84 ± 0.05	-
1.47	21520 ± 3940	15540 ± 450	10.46 ± 0.01	8.68 ± 0.09	6.79 ± 0.05	-
1.96	16340 ± 3810	15330 ± 560	10.43 ± 0.01	8.61 ± 0.10	6.76 ± 0.05	-
2.44	16230 ± 3180	15650 ± 580	10.41 ± 0.01	8.61 ± 0.07	6.68 ± 0.04	-
2.93	13220 ± 2720	14640 ± 500	10.39 ± 0.01	8.56 ± 0.08	6.69 ± 0.04	-
3.42	17720 ± 3410	14570 ± 430	10.38 ± 0.01	8.67 ± 0.09	6.68 ± 0.04	-
3.91	17130 ± 3000	13940 ± 380	10.39 ± 0.01	8.63 ± 0.08	6.67 ± 0.05	-
4.40	13920 ± 2750	13450 ± 510	10.41 ± 0.01	8.58 ± 0.08	6.66 ± 0.04	-
4.89	14590 ± 2790	12460 ± 420	10.38 ± 0.01	8.60 ± 0.08	6.67 ± 0.04	-
5.38	13220 ± 2590	12040 ± 330	10.38 ± 0.01	8.54 ± 0.08	6.65 ± 0.04	-
5.87	11530 ± 2120	11990 ± 360	10.41 ± 0.01	8.52 ± 0.08	6.69 ± 0.04	-
6.36	13560 ± 2370	11230 ± 380	10.41 ± 0.01	8.58 ± 0.08	6.70 ± 0.04	-
6.85	12590 ± 2430	11590 ± 330	10.44 ± 0.01	8.60 ± 0.08	6.75 ± 0.04	5.49 ± 0.08
7.33	13920 ± 2640	11550 ± 320	10.45 ± 0.01	8.59 ± 0.09	6.73 ± 0.04	5.58 ± 0.06
7.82	12980 ± 2550	11460 ± 300	10.45 ± 0.01	8.54 ± 0.08	6.76 ± 0.04	5.62 ± 0.06
8.31	14430 ± 2990	11740 ± 360	10.45 ± 0.01	8.58 ± 0.09	6.74 ± 0.05	5.62 ± 0.08
8.80	11570 ± 2240	11280 ± 260	10.45 ± 0.01	8.54 ± 0.07	6.76 ± 0.05	5.59 ± 0.08
9.29	12860 ± 2690	11410 ± 290	10.47 ± 0.01	8.51 ± 0.07	6.78 ± 0.04	5.64 ± 0.07
9.78	11830 ± 2260	11230 ± 290	10.53 ± 0.01	8.54 ± 0.07	6.84 ± 0.05	5.65 ± 0.06
10.27	11370 ± 2190	11580 ± 240	10.58 ± 0.01	8.54 ± 0.06	6.94 ± 0.04	5.72 ± 0.06
10.76	11420 ± 2370	12040 ± 300	10.65 ± 0.01	8.53 ± 0.08	6.95 ± 0.05	5.78 ± 0.08
11.25	9680 ± 1940	11540 ± 310	10.70 ± 0.01	8.52 ± 0.07	7.02 ± 0.04	5.90 ± 0.06
11.74	9780 ± 2220	11760 ± 260	10.75 ± 0.01	8.50 ± 0.08	7.06 ± 0.05	5.92 ± 0.06
12.22	10760 ± 2370	11510 ± 230	10.80 ± 0.01	8.52 ± 0.07	7.13 ± 0.04	6.05 ± 0.05
12.71	9470 ± 2020	10980 ± 240	10.84 ± 0.01	8.48 ± 0.08	7.16 ± 0.04	6.00 ± 0.05

**Figure A1.** Plasma diagnostic plots for the individual analyzed components. The labeled diagnostics correspond to those discussed in Sec. 4.1.

**Table A2.** Spatial distribution of physical conditions and ionic abundances along HH 204 as a function of the distance from the bowshock. Values derived from the red arm spectrum.

Distance (mpc)	$T_e(\text{[N II]})$ (K)	$T_e(\text{[S III]})$ (K)	$\text{He}^+ (\lambda 5876)$	$\text{He}^+ (\lambda 6678)$	$\text{N}^+$ log. units with $n(\text{H})=12$	$\text{O}^+ (\text{RLs})$	$\text{S}^+$	$\text{S}^{2+}$
0.29	$8780 \pm 310$	$9150 \pm 190$	$10.41 \pm 0.01$	$10.57 \pm 0.03$	$7.79 \pm 0.06$	$8.68 \pm 0.15$	$6.82 \pm 0.09$	$6.84 \pm 0.03$
0.66	$8970 \pm 340$	$8780 \pm 180$	$10.43 \pm 0.01$	$10.51 \pm 0.03$	$7.75 \pm 0.05$	$8.87 \pm 0.11$	$6.77 \pm 0.08$	$6.90 \pm 0.03$
1.02	$8670 \pm 280$	$9140 \pm 210$	$10.43 \pm 0.01$	$10.50 \pm 0.02$	$7.80 \pm 0.05$	-	$6.82 \pm 0.09$	$6.83 \pm 0.03$
1.38	$8920 \pm 300$	$9500 \pm 220$	$10.42 \pm 0.01$	$10.48 \pm 0.02$	$7.75 \pm 0.05$	$8.75 \pm 0.12$	$6.78 \pm 0.08$	$6.77 \pm 0.03$
1.74	$9100 \pm 290$	$9390 \pm 190$	$10.42 \pm 0.01$	$10.43 \pm 0.02$	$7.71 \pm 0.04$	-	$6.73 \pm 0.07$	$6.78 \pm 0.02$
2.10	$8860 \pm 290$	$9050 \pm 200$	$10.41 \pm 0.01$	$10.48 \pm 0.02$	$7.73 \pm 0.05$	$8.57 \pm 0.15$	$6.73 \pm 0.08$	$6.82 \pm 0.02$
2.46	$8980 \pm 220$	$9290 \pm 210$	$10.39 \pm 0.01$	$10.45 \pm 0.02$	$7.73 \pm 0.04$	$8.80 \pm 0.09$	$6.74 \pm 0.06$	$6.82 \pm 0.03$
2.83	$8850 \pm 220$	$9420 \pm 170$	$10.37 \pm 0.01$	$10.43 \pm 0.02$	$7.73 \pm 0.03$	$8.70 \pm 0.09$	$6.72 \pm 0.07$	$6.78 \pm 0.02$
3.19	$8750 \pm 230$	$9250 \pm 180$	$10.37 \pm 0.01$	$10.39 \pm 0.02$	$7.75 \pm 0.04$	$8.72 \pm 0.07$	$6.76 \pm 0.07$	$6.77 \pm 0.03$
3.55	$8790 \pm 190$	$9410 \pm 180$	$10.36 \pm 0.01$	$10.43 \pm 0.02$	$7.75 \pm 0.04$	$8.68 \pm 0.07$	$6.79 \pm 0.07$	$6.75 \pm 0.02$
3.91	$8860 \pm 260$	$9410 \pm 180$	$10.36 \pm 0.01$	$10.42 \pm 0.02$	$7.75 \pm 0.04$	$8.66 \pm 0.07$	$6.78 \pm 0.07$	$6.74 \pm 0.03$
4.27	$8900 \pm 230$	$9390 \pm 190$	$10.37 \pm 0.01$	$10.42 \pm 0.02$	$7.74 \pm 0.04$	$8.74 \pm 0.06$	$6.75 \pm 0.06$	$6.74 \pm 0.03$
4.64	$8800 \pm 230$	$9430 \pm 190$	$10.36 \pm 0.01$	$10.41 \pm 0.02$	$7.75 \pm 0.04$	$8.79 \pm 0.06$	$6.72 \pm 0.06$	$6.73 \pm 0.02$
5.00	$8760 \pm 230$	$9400 \pm 190$	$10.34 \pm 0.01$	$10.40 \pm 0.02$	$7.74 \pm 0.04$	$8.74 \pm 0.07$	$6.72 \pm 0.06$	$6.72 \pm 0.03$
5.36	$8960 \pm 220$	$9480 \pm 190$	$10.36 \pm 0.01$	$10.41 \pm 0.02$	$7.71 \pm 0.04$	$8.72 \pm 0.06$	$6.66 \pm 0.06$	$6.71 \pm 0.02$
5.72	$8880 \pm 210$	$9310 \pm 190$	$10.36 \pm 0.01$	$10.42 \pm 0.02$	$7.72 \pm 0.04$	$8.71 \pm 0.06$	$6.63 \pm 0.08$	$6.74 \pm 0.03$
6.08	$8800 \pm 220$	$9330 \pm 180$	$10.36 \pm 0.01$	$10.42 \pm 0.02$	$7.74 \pm 0.04$	$8.73 \pm 0.05$	$6.67 \pm 0.06$	$6.74 \pm 0.03$
6.44	$8810 \pm 220$	$9280 \pm 180$	$10.38 \pm 0.01$	$10.42 \pm 0.02$	$7.73 \pm 0.04$	$8.64 \pm 0.06$	$6.66 \pm 0.07$	$6.76 \pm 0.02$
6.81	$8760 \pm 210$	$9240 \pm 210$	$10.39 \pm 0.01$	$10.43 \pm 0.02$	$7.72 \pm 0.04$	$8.65 \pm 0.06$	$6.61 \pm 0.07$	$6.76 \pm 0.03$
7.17	$8790 \pm 240$	$9290 \pm 200$	$10.40 \pm 0.01$	$10.44 \pm 0.02$	$7.70 \pm 0.04$	$8.73 \pm 0.04$	$6.61 \pm 0.06$	$6.75 \pm 0.03$
7.53	$8840 \pm 220$	$9480 \pm 170$	$10.42 \pm 0.01$	$10.45 \pm 0.02$	$7.70 \pm 0.03$	$8.56 \pm 0.06$	$6.57 \pm 0.06$	$6.71 \pm 0.02$
7.89	$8830 \pm 250$	$9500 \pm 180$	$10.40 \pm 0.01$	$10.45 \pm 0.01$	$7.68 \pm 0.04$	$8.57 \pm 0.06$	$6.56 \pm 0.07$	$6.71 \pm 0.02$
8.25	$8800 \pm 270$	$9410 \pm 190$	$10.41 \pm 0.01$	$10.46 \pm 0.02$	$7.71 \pm 0.04$	$8.62 \pm 0.06$	$6.58 \pm 0.07$	$6.73 \pm 0.02$
8.61	$8830 \pm 220$	$9360 \pm 200$	$10.41 \pm 0.01$	$10.46 \pm 0.02$	$7.70 \pm 0.04$	$8.64 \pm 0.05$	$6.56 \pm 0.07$	$6.75 \pm 0.02$
8.98	$8870 \pm 230$	$9370 \pm 160$	$10.42 \pm 0.02$	$10.47 \pm 0.02$	$7.70 \pm 0.03$	$8.56 \pm 0.10$	$6.53 \pm 0.06$	$6.77 \pm 0.02$
9.34	$8920 \pm 210$	$9220 \pm 180$	$10.44 \pm 0.01$	$10.48 \pm 0.02$	$7.70 \pm 0.03$	$8.61 \pm 0.06$	$6.53 \pm 0.06$	$6.80 \pm 0.02$
9.70	$8860 \pm 210$	$9410 \pm 200$	$10.45 \pm 0.01$	$10.49 \pm 0.01$	$7.70 \pm 0.04$	$8.63 \pm 0.05$	$6.52 \pm 0.06$	$6.77 \pm 0.03$
10.06	$8800 \pm 210$	$9570 \pm 160$	$10.47 \pm 0.01$	$10.51 \pm 0.01$	$7.69 \pm 0.03$	$8.60 \pm 0.05$	$6.47 \pm 0.05$	$6.74 \pm 0.02$
10.42	$8730 \pm 210$	$9740 \pm 210$	$10.49 \pm 0.01$	$10.53 \pm 0.01$	$7.69 \pm 0.04$	$8.62 \pm 0.06$	$6.41 \pm 0.07$	$6.70 \pm 0.03$
10.79	$8850 \pm 210$	$9900 \pm 200$	$10.54 \pm 0.01$	$10.59 \pm 0.01$	$7.65 \pm 0.04$	$8.56 \pm 0.07$	$6.34 \pm 0.07$	$6.68 \pm 0.03$
11.15	$8770 \pm 210$	$9890 \pm 220$	$10.59 \pm 0.01$	$10.62 \pm 0.02$	$7.65 \pm 0.04$	$8.56 \pm 0.08$	$6.27 \pm 0.07$	$6.67 \pm 0.03$
11.51	$8820 \pm 210$	$9680 \pm 210$	$10.63 \pm 0.01$	$10.65 \pm 0.01$	$7.64 \pm 0.04$	$8.77 \pm 0.11$	$6.23 \pm 0.06$	$6.72 \pm 0.02$
11.87	$8720 \pm 220$	$9690 \pm 190$	$10.68 \pm 0.01$	$10.71 \pm 0.01$	$7.64 \pm 0.04$	$8.60 \pm 0.07$	$6.24 \pm 0.06$	$6.73 \pm 0.03$
12.23	$8740 \pm 200$	$9840 \pm 200$	$10.73 \pm 0.01$	$10.75 \pm 0.02$	$7.64 \pm 0.04$	$8.75 \pm 0.06$	$6.24 \pm 0.08$	$6.72 \pm 0.02$
12.59	$8860 \pm 190$	$9750 \pm 210$	$10.76 \pm 0.01$	$10.79 \pm 0.01$	$7.60 \pm 0.03$	$8.68 \pm 0.09$	$6.18 \pm 0.06$	$6.73 \pm 0.03$
12.96	$8980 \pm 200$	$9720 \pm 190$	$10.80 \pm 0.01$	$10.82 \pm 0.01$	$7.57 \pm 0.03$	$8.41 \pm 0.13$	$6.12 \pm 0.07$	$6.74 \pm 0.02$
13.32	$8320 \pm 270$	$9880 \pm 200$	$10.82 \pm 0.01$	$10.85 \pm 0.01$	$7.53 \pm 0.03$	$8.67 \pm 0.09$	$6.07 \pm 0.05$	$6.70 \pm 0.02$



**Table A3.** Further ionic abundances along HH 204 as a function of the distance from the bowshock. Values derived from the red arm spectrum.

Distance (mpc)	Cl <sup>+</sup>	Cl <sup>2+</sup>	Ar <sup>2+</sup>	Ca <sup>+</sup>	Cr <sup>+</sup>	Fe <sup>+</sup>	Fe <sup>2+</sup>	Ni <sup>+</sup>	Ni <sup>2+</sup>
log. units with $n(\text{H})=12$									
0.29	4.93 ± 0.05	4.63 ± 0.08	5.66 ± 0.05	3.64 ± 0.05	4.57 ± 0.06	6.35 ± 0.04	6.46 ± 0.06	5.08 ± 0.03	5.05 ± 0.07
0.66	4.92 ± 0.04	4.83 ± 0.08	5.66 ± 0.04	3.66 ± 0.05	4.59 ± 0.06	6.35 ± 0.04	6.42 ± 0.06	5.09 ± 0.03	5.07 ± 0.06
1.02	4.94 ± 0.03	4.74 ± 0.05	5.70 ± 0.04	3.64 ± 0.05	4.71 ± 0.05	6.32 ± 0.05	6.49 ± 0.05	5.08 ± 0.03	5.10 ± 0.05
1.38	4.84 ± 0.04	4.67 ± 0.06	5.64 ± 0.04	3.47 ± 0.06	4.59 ± 0.05	6.27 ± 0.05	6.45 ± 0.06	5.00 ± 0.03	5.06 ± 0.06
1.74	4.80 ± 0.04	4.72 ± 0.04	5.59 ± 0.03	3.54 ± 0.05	4.49 ± 0.04	6.17 ± 0.04	6.40 ± 0.05	4.97 ± 0.03	5.00 ± 0.06
2.10	4.82 ± 0.04	4.86 ± 0.05	5.61 ± 0.04	3.46 ± 0.04	4.53 ± 0.04	6.23 ± 0.05	6.43 ± 0.05	5.00 ± 0.03	5.04 ± 0.05
2.46	4.84 ± 0.04	4.84 ± 0.04	5.60 ± 0.03	3.53 ± 0.05	4.55 ± 0.04	6.26 ± 0.04	6.42 ± 0.04	5.03 ± 0.03	5.07 ± 0.05
2.83	4.82 ± 0.03	4.83 ± 0.04	5.59 ± 0.03	3.51 ± 0.04	4.58 ± 0.03	6.28 ± 0.03	6.46 ± 0.04	5.02 ± 0.03	5.03 ± 0.04
3.19	4.83 ± 0.03	4.80 ± 0.05	5.58 ± 0.03	3.52 ± 0.04	4.59 ± 0.04	6.28 ± 0.03	6.49 ± 0.05	5.07 ± 0.03	5.08 ± 0.05
3.55	4.83 ± 0.03	4.71 ± 0.05	5.56 ± 0.03	3.57 ± 0.04	4.58 ± 0.04	6.28 ± 0.03	6.46 ± 0.04	5.07 ± 0.02	5.05 ± 0.04
3.91	4.83 ± 0.03	4.73 ± 0.04	5.54 ± 0.04	3.56 ± 0.04	4.53 ± 0.04	6.29 ± 0.03	6.47 ± 0.05	5.06 ± 0.03	5.06 ± 0.05
4.27	4.81 ± 0.03	4.69 ± 0.05	5.55 ± 0.03	3.54 ± 0.04	4.49 ± 0.04	6.30 ± 0.03	6.46 ± 0.05	5.05 ± 0.03	5.09 ± 0.05
4.64	4.81 ± 0.03	4.73 ± 0.04	5.56 ± 0.03	3.54 ± 0.03	4.44 ± 0.03	6.32 ± 0.03	6.49 ± 0.04	5.03 ± 0.02	5.11 ± 0.04
5.00	4.80 ± 0.03	4.71 ± 0.04	5.56 ± 0.03	3.55 ± 0.04	4.46 ± 0.04	6.32 ± 0.04	6.50 ± 0.04	5.02 ± 0.03	5.11 ± 0.05
5.36	4.76 ± 0.04	4.68 ± 0.04	5.53 ± 0.03	3.50 ± 0.04	4.41 ± 0.03	6.27 ± 0.03	6.46 ± 0.04	4.99 ± 0.03	5.07 ± 0.04
5.72	4.77 ± 0.03	4.75 ± 0.04	5.55 ± 0.03	3.54 ± 0.04	4.36 ± 0.04	6.27 ± 0.03	6.49 ± 0.04	5.00 ± 0.02	5.12 ± 0.04
6.08	4.76 ± 0.03	4.71 ± 0.05	5.57 ± 0.03	3.55 ± 0.03	4.37 ± 0.04	6.29 ± 0.03	6.51 ± 0.04	5.00 ± 0.02	5.14 ± 0.04
6.44	4.77 ± 0.03	4.76 ± 0.04	5.58 ± 0.03	3.56 ± 0.04	4.34 ± 0.03	6.27 ± 0.03	6.50 ± 0.04	4.99 ± 0.02	5.13 ± 0.04
6.81	4.75 ± 0.03	4.76 ± 0.04	5.60 ± 0.03	3.58 ± 0.04	4.30 ± 0.04	6.26 ± 0.03	6.51 ± 0.04	4.96 ± 0.02	5.12 ± 0.04
7.17	4.71 ± 0.03	4.79 ± 0.04	5.59 ± 0.03	3.55 ± 0.04	4.23 ± 0.04	6.20 ± 0.04	6.48 ± 0.05	4.92 ± 0.03	5.11 ± 0.05
7.53	4.69 ± 0.03	4.76 ± 0.04	5.60 ± 0.03	3.50 ± 0.03	4.18 ± 0.03	6.15 ± 0.03	6.49 ± 0.04	4.88 ± 0.02	5.12 ± 0.04
7.89	4.65 ± 0.03	4.71 ± 0.04	5.59 ± 0.03	3.52 ± 0.03	4.22 ± 0.04	6.12 ± 0.04	6.48 ± 0.05	4.87 ± 0.02	5.13 ± 0.04
8.25	4.67 ± 0.03	4.76 ± 0.04	5.61 ± 0.03	3.55 ± 0.03	4.18 ± 0.04	6.17 ± 0.04	6.52 ± 0.05	4.90 ± 0.03	5.15 ± 0.04
8.61	4.72 ± 0.03	4.77 ± 0.03	5.61 ± 0.03	3.58 ± 0.04	4.25 ± 0.04	6.20 ± 0.03	6.50 ± 0.04	4.92 ± 0.02	5.14 ± 0.04
8.98	4.75 ± 0.04	4.74 ± 0.03	5.61 ± 0.03	3.59 ± 0.04	4.23 ± 0.04	6.21 ± 0.04	6.51 ± 0.04	4.92 ± 0.02	5.18 ± 0.04
9.34	4.74 ± 0.03	4.81 ± 0.03	5.61 ± 0.03	3.60 ± 0.03	4.21 ± 0.03	6.21 ± 0.04	6.49 ± 0.04	4.92 ± 0.02	5.16 ± 0.04
9.70	4.70 ± 0.03	4.79 ± 0.04	5.63 ± 0.03	3.56 ± 0.03	4.20 ± 0.04	6.19 ± 0.03	6.51 ± 0.04	4.90 ± 0.02	5.17 ± 0.04
10.06	4.67 ± 0.03	4.78 ± 0.03	5.64 ± 0.03	3.53 ± 0.04	4.13 ± 0.04	6.13 ± 0.03	6.52 ± 0.04	4.84 ± 0.02	5.18 ± 0.04
10.42	4.58 ± 0.04	4.76 ± 0.04	5.65 ± 0.03	3.48 ± 0.04	3.98 ± 0.04	6.01 ± 0.03	6.54 ± 0.05	4.75 ± 0.02	5.15 ± 0.04
10.79	4.48 ± 0.03	4.68 ± 0.04	5.66 ± 0.03	3.43 ± 0.04	3.72 ± 0.07	5.82 ± 0.03	6.51 ± 0.04	4.64 ± 0.02	5.12 ± 0.04
11.15	4.44 ± 0.03	4.74 ± 0.04	5.72 ± 0.03	3.39 ± 0.04	3.66 ± 0.09	5.72 ± 0.05	6.53 ± 0.04	4.52 ± 0.03	5.16 ± 0.04
11.51	4.42 ± 0.04	4.80 ± 0.03	5.76 ± 0.03	3.34 ± 0.04	3.47 ± 0.10	5.65 ± 0.05	6.52 ± 0.05	4.45 ± 0.03	5.18 ± 0.04
11.87	4.42 ± 0.04	4.81 ± 0.03	5.82 ± 0.03	3.24 ± 0.05	-	5.58 ± 0.05	6.53 ± 0.05	4.38 ± 0.03	5.17 ± 0.04
12.23	4.37 ± 0.03	4.78 ± 0.04	5.86 ± 0.04	3.26 ± 0.05	-	5.62 ± 0.05	6.52 ± 0.05	4.34 ± 0.02	5.17 ± 0.04
12.59	4.38 ± 0.04	4.76 ± 0.04	5.88 ± 0.03	3.26 ± 0.04	3.50 ± 0.12	5.54 ± 0.05	6.52 ± 0.03	4.28 ± 0.02	5.17 ± 0.04
12.96	4.33 ± 0.12	4.82 ± 0.04	5.90 ± 0.03	3.20 ± 0.05	3.43 ± 0.13	5.58 ± 0.05	6.49 ± 0.04	4.24 ± 0.03	5.13 ± 0.04
13.32	4.29 ± 0.04	4.73 ± 0.04	5.93 ± 0.02	3.22 ± 0.05	-	5.42 ± 0.07	6.47 ± 0.03	4.23 ± 0.03	5.14 ± 0.04

**Table A4.** Atomic data set used for collisionally excited lines.

Ion	Transition Probabilities	Collision Strengths
O <sup>0</sup>	Wiese et al. (1996)	Bhatia & Kastner (1995)
O <sup>+</sup>	Froese Fischer & Tachiev (2004)	Kisieliuss et al. (2009)
O <sup>2+</sup>	Wiese et al. (1996), Storey & Zeippen (2000)	Storey et al. (2014)
N <sup>+</sup>	Froese Fischer & Tachiev (2004)	Tayal (2011)
Ne <sup>2+</sup>	McLaughlin et al. (2011)	McLaughlin et al. (2011)
S <sup>+</sup>	Podobedova et al. (2009)	Tayal & Zatsarinny (2010)
S <sup>2+</sup>	Podobedova et al. (2009)	Grieve et al. (2014)
Cl <sup>+</sup>	Mendoza & Zeippen (1983)	Tayal (2004)
Cl <sup>2+</sup>	Fritzsche et al. (1999)	Butler & Zeippen (1989)
Ar <sup>2+</sup>	Mendoza (1983), Kaufman & Sugar (1986)	Galavis, Mendoza & Zeippen (1995)
Ar <sup>3+</sup>	Mendoza & Zeippen (1982)	Ramsbottom & Bell (1997)
Fe <sup>+</sup>	Bautista et al. (2015)	Bautista et al. (2015)
Fe <sup>2+</sup>	Quinet (1996), Johansson et al. (2000)	Zhang, Hong Lin (1996)
Fe <sup>3+</sup>	Froese Fischer et al. (2008)	Zhang & Pradhan (1997)
Ni <sup>+</sup>	Quinet & Le Dourneuf (1996), Nussbaumer & Storey (1982)	Bautista (2004)
Ni <sup>2+</sup>	Bautista (2001)	Bautista (2001)
Ca <sup>+</sup>	Meléndez et al. (2007)	Meléndez et al. (2007)
Cr <sup>+</sup>	Tayal & Zatsarinny (2020)	Tayal & Zatsarinny (2020)

**Table A5.** Effective recombination coefficients used for recombination lines.

Ion	Reference
H <sup>+</sup>	<a href="#">Storey &amp; Hummer (1995)</a>
He <sup>+</sup>	<a href="#">Porter et al. (2012, 2013)</a>
O <sup>+</sup>	<a href="#">Pequignot et al. (1991)</a>
O <sup>2+</sup>	<a href="#">Storey et al. (2017)</a>
C <sup>2+</sup>	<a href="#">Davey et al. (2000)</a>

**Table A6.** Comparison of the observed [Fe III] intensity ratios in HH 204 and theoretical ones predicted by the transition probabilities of [Quinet \(1996\)](#) and [Johansson et al. \(2000\)](#).

Line ratio	HH 204	Prediction
3240/3286	$3.63 \pm 0.81$	3.60
3240/3319	$3.63 \pm 0.86$	5.06
3240/8729*	$11.35 \pm 1.06$	11.87
3335/3357	$1.16 \pm 0.20$	1.18
3335/8838**	$6.15 \pm 1.00$	4.93
4607/4702	$0.18 \pm 0.01$	0.17
4607/4770	$0.51 \pm 0.01$	0.51
4667/4734	$0.29 \pm 0.01$	0.28
4667/4778	$0.60 \pm 0.03$	0.57
4658/4755	$5.33 \pm 0.15$	5.49
4881/4987	$6.07 \pm 0.17$	5.76
5011/5085	$5.85 \pm 0.32$	5.94
5271/5412	$10.75 \pm 0.39$	11.01

\* The emission of [Fe III] $\lambda$ 8728.84 from HH 204 was deblended from the nebular component of [C I] $\lambda$ 8727.13.

\*\* The emission of [Fe III] $\lambda$ 8838.14 was deblended from a sky feature.

**Table A7.** Comparison of the observed [Fe II] intensity ratios in HH 204 and theoretical ones predicted by the transition probabilities of [Bautista et al. \(2015\)](#).

Line ratio	HH 204	Prediction
9051.95/9399.04	$5.45 \pm 0.48$	5.49
9051.95/7926.88	$18.84 \pm 1.99$	6.91
8891.93/9226.63	$1.71 \pm 0.11$	1.80
8891.93/7874.23	$28.58 \pm 4.15$	10.64
8891.93/7686.93	$3.85 \pm 0.22$	1.48
9267.56/9033.49*	$1.33 \pm 0.09$	1.28
9267.56/7733.13*	$11.72 \pm 1.37$	5.08

\* [Fe II] $\lambda$ 9267.56 was deblended from a sky emission.